EBioMedicine 61 (2020) 103050

Contents lists available at ScienceDirect

EBioMedicine

journal homepage: www.elsevier.com/locate/ebiom

Research paper

Impaired flickering of the permeability transition pore causes SPG7 spastic paraplegia

Irene Sambri[a,#], Filomena Massa[a,#], Francesca Gullo[b], Simone Meneghini[b], Laura Cassina[c], Michela Carraro[d], Giorgia Dina[c], Angelo Quattrini[c], Lorenzo Patanella[a], Annamaria Carissimo[a,g], Antonella Iuliano[a], Filippo Santorelli[e], Franca Codazzi[f], Fabio Grohovaz[f], Paolo Bernardi[d], Andrea Becchetti[b], Giorgio Casari[a,f,*]

[a] Telethon Institute of Genetics and Medicine (TIGEM), Pozzuoli-Naples, Italy
[b] University of Milano-Bicocca, Milan, Italy
[c] San Raffaele Scientific Institute, Milan, Italy
[d] University of Padua, Padua, Italy
[e] RCCS Fondazione Stella Maris, Pisa, Italy
[f] Vita-Salute San Raffaele University, Milan, Italy
[g] Institute for Applied Mathematics 'Mauro Picone', National Research Council, Naples, Italy

ARTICLE INFO

Article History:
Received 15 May 2020
Revised 14 September 2020
Accepted 22 September 2020
Available online 9 October 2020

Keywords:
Hereditary spastic paraplegia
Paraplegin
SPG7
Mitochondria
Permeability transition pore
Synaptic vesicles

ABSTRACT

Background: Mutations of the mitochondrial protein paraplegin cause hereditary spastic paraplegia type 7 (SPG7), a so-far untreatable degenerative disease of the upper motoneuron with still undefined pathomechanism.
The intermittent mitochondrial permeability transition pore (mPTP) opening, called flickering, is an essential process that operates to maintain mitochondrial homeostasis by reducing intra-matrix Ca^{2+} and reactive oxygen species (ROS) concentration, and is critical for efficient synaptic function.
Methods: We use a fluorescence-based approach to measure mPTP flickering in living cells and biochemical and molecular biology techniques to dissect the pathogenic mechanism of SPG7. In the SPG7 animal model we evaluate the potential improvement of the motor defect, neuroinflammation and neurodegeneration by means of an mPTP inducer, the benzodiazepine Bz-423.
Findings: We demonstrate that paraplegin is required for efficient transient opening of the mPTP, that is impaired in both SPG7 patients-derived fibroblasts and primary neurons from *Spg7*$^{-/-}$ mice. We show that dysregulation of mPTP opening at the pre-synaptic terminal impairs neurotransmitter release leading to ineffective synaptic transmission. Lack of paraplegin impairs mPTP flickering by a mechanism involving increased expression and activity of sirtuin3, which promotes deacetylation of cyclophilin D, thus hampering mPTP opening. Pharmacological treatment with Bz-423, which bypasses the activity of CypD, normalizes synaptic transmission and rescues the motor impairment of the SPG7 mouse model.
Interpretation: mPTP targeting opens a new avenue for the potential therapy of this form of spastic paraplegia.
Funding: Telethon Foundation grant (TGMGCSBX16TT); Dept. of Defense, US Army, grant W81XWH-18−1−0001

© 2020 The Authors. Published by Elsevier B.V. This is an open access article under the CC BY-NC-ND license (http://creativecommons.org/licenses/by-nc-nd/4.0/)

1. Introduction

Hereditary spastic paraplegia (HSP) is a large group of rare genetic neurological diseases characterized by degeneration of the corticospinal tract [1]. Lower limb spasticity and weakness, the more common initial and usually progressing symptoms, may have their onset from childhood to the third-fourth and even fifth decade [2].

The genetics of HSP is quite complex both in terms of inheritance pattern – autosomal dominant, autosomal recessive, X-linked, and mitochondrial inheritance have all been reported – and of the extraordinary genetic heterogeneity involving more than 80 different loci, with 58 already identified HSP genes [3].

* Corresponding author.
E-mail address: casari.giorgio@hsr.it (G. Casari).
# These authors contributed equally.

https://doi.org/10.1016/j.ebiom.2020.103050
2352-3964/© 2020 The Authors. Published by Elsevier B.V. This is an open access article under the CC BY-NC-ND license (http://creativecommons.org/licenses/by-nc-nd/4.0/)

RESEARCH IN CONTEXT

Evidence before this study

Mutations of the SPG7 gene, which encodes the mitochondrial protein paraplegin, are known to cause a recessive form of hereditary spastic paraplegia (SPG7) in the past two decades. Nonetheless, the molecular mechanism leading to this form of neurodegeneration is still unclear.

The permeability transition pore (mPTP) on the inner mitochondrial can trigger cell death in response to increased mitochondrial calcium by massively opening and discharge matrix content into the cytoplasm. Differently from this permanent and high conductance mode, the mPTP can open in a physiological and low conductance way to maintain mitochondrial calcium homeostasis.

Added value of this study

This work reports for the first time a human disease associated to impairment of the low conductance opening of the mPTP and discloses the intimate molecular pathomechanism leading to SPG7 spastic paraplegia. The available mutant animal model contributes an in vivo proof of principle for the pharmacological therapy of this disease.

Implications of all the available evidence

The novelty of functionally linking the mPTP to SPG7 spastic paraplegia opens to mPTP modulation as a prospective strategy for SPG7 treatment. The benzodiazepine Bz-423 as mPTP opening inducers can represent a pharmacological approach to relieve specific mitochondrial conditions such as the SPG7 neurodegeneration.

Two decades ago, the *SPG7* gene, which encodes paraplegin, was identified as responsible for the first identified autosomal recessive form of HSP (SPG7)[4]. The phenotype of the *Spg7* knock-out mouse model matches the clinical feature of SPG7 patients, with mild and slowly progressive motor impairment associated with distal axonopathy of spinal and peripheral axons [5] .

Paraplegin is a mitochondrial protein belonging to the AAA-protease superfamily (ATPases associated with a variety of cellular activities), which assembles into hetero-oligomers with its homolog AFG3L2 in the inner mitochondrial membrane [6]. Contrary to paraplegin, AFG3L2 is also able to form homo-complexes; both hetero- and homocomplexes constitute active *m*-AAA proteases.

Through selective degradation of non-assembled and damaged proteins, the *m*-AAA complex exerts protein quality control surveillance in the inner membrane [7], while through its chaperone-like activity participates in the assembly of respiratory chain complexes [8-10]. Furthermore, the *m*-AAA complex mediates the proteolytic activation of substrates such as the nuclear-encoded subunit of mitochondrial ribosome MrpL32, the regulator of mitochondrial fusion protein OPA1 [11]· [12].

Dominant mutations of AFG3L2, the paraplegin partner in the *m*-AAA complex, are responsible for spinocerebellar ataxia type 28 (SCA28) [13]. Extensive investigation of AFG3L2 association with SCA28 pathogenesis points to a role in the control of organelle fragmentation and Ca^{2+} buffering in Purkinje neurons [10]· [14-17]. A third very rare and severe disease, SPAX5, has been associated with recessive mutations of AFG3L2 and recalls features of both SCA28 and SPG7 [18].

Although the molecular mechanism leading to primary motoneuron degeneration in SPG7 is still missing, the hypothesis of a mitochondrial pathogenesis is supported by the evidence of respiratory complex I-deficiency and partial mitochondrial DNA depletion in SPG7 patient cells [9]· [19]· [20].

Mitochondria are important for the maintenance of neuron integrity and function [21]; indeed, diseases caused by mitochondrial failure often display a neurodegenerative component affecting the central or peripheral nervous system [22]. Of note, mitochondrial defects are frequently observed also in peripheral samples collected from patients with neurodegenerative disorders [23].

The intimate involvement of mitochondria in controlling neurotransmission has been demonstrated in several diseases, such as in GDAP1-related Charcot-Marie-Tooth, where dysfunctional mitochondria cause impairment of Ca^{2+} homeostasis at axonal terminals [24]; in epilepsy, where they contribute to dysregulation of excitability [25]; as well as in Alzheimer [26], and Parkinson diseases [27].

A key effector of mitochondrial dysfunction is an increased permeability of the inner mitochondrial membrane (IMM), triggered by matrix Ca^{2+}, phosphate (Pi) and reactive oxygen species (ROS) through opening of the mitochondrial permeability transition pore (mPTP), a channel regulated by the acetylation/deacetylation ratio of the matrix protein cyclophilin D (CypD), which binds to the OSCP subunit of ATP synthase and favors mPTP opening [28].

The mPTP can open in low or high conductance modes. Intermittent opening/closing of the pore (flickering) is physiological and essential for mitochondrial Ca^{2+}homeostasis, as it controls Ca^{2+}release, finely tuning its concentration in the matrix [29–35]. By contrast, high conductance, long-lasting opening is a major cell death pathway driven by the organelle, as it causes IMM depolarization with massive mitochondrial Ca^{2+} release, inhibition of respiration, cessation of ATP synthesis, and matrix swelling, eventually leading to cytochrome C, AIF and endonuclease G release, with consequent cell death [36].

Here we show that paraplegin mutations increase expression of surtuin 3, and push its activity leading to lower levels of acetylated CypD, finally result in blunting the physiological, transient openings of the mPTP with detrimental consequences on synaptic transmission. Pharmacological activation of mPTP, bypassing the deficiency of acetylated CypD, restores synaptic transmission and prevents the onset of motor impairment in the SPG7 mouse model. We finally provide the first example of a human disease caused by impaired pore opening and demonstrate the actionability of mPTP as potential therapeutic target for SPG7.

2. Methods

2.1. Cell cultures

Fibroblasts were cultured in Dulbecco's Modified Eagle Medium (Cat# 41,965–039 EuroClone, Milan, Italy) containing 20% fetal bovine serum (FBS) (Cat# ECS0186L EuroClone, Milan, Italy), 1% L-glutamine (Cat# ECB3000D EuroClone, Milan, Italy), and 1% antibiotics (penicillin/streptomycin (PS)) (Cat# ECB3001D EuroClone, Milan, Italy); HEK293 cells were grown in high glucose DMEM (Cat# ECM0728L EuroClone, Milan, Italy) supplemented with 10% FBS and 1% PS at 37 °C and 5% CO2. All cells were splitted upon reaching of confluence, by rinsing the monolayer twice with sterile Phosphate-Buffered Saline (Cat# ECB400L PBS, EuroClone, Milan, Italy) and exposing cells to 0.25% Trypsin-EDTA (Cat# ECB3052D EuroClone, Milan, Italy) for 2–3 min. Detached cells were centrifuged to remove Trypsin from the media and then plated.

2.2. Generation of SPG7 knockout HEK293 cells by CRISPR/Cas9 genome editing

We generated *SPG7* knockout HEK293 cells by CRISPR/Cas9 Genome Editing. Briefly, gRNA guides (G1: ACATCTGGTCGTCCCGC TCA, and G2: CCGGGTCCTCGGCCGCTGTG), targeting exon 4 and exon

1 of the human *SPG7* gene respectively, were cloned in the pCas-Guide-EF1a-GFP plasmid (GE100018, OriGene Technologies, Inc, Rockville, USA). The plasmid expresses a CMV-driven codon-optimized Cas9 and EF1a promoter driven GFP. HEK293 cells were transfected with the indicated plasmids using Lipofectamine (Life Technologies, Carlsbad, CA, USA), 48 h after transfection single cells were sorted for GFP expression and collected in 96 multiwell plate for each gRNA guide for single clone isolation. *SPG7* KO clones were screened by western blot using paraplegin-specific antibody.

2.3. Cell permeabilization and Ca^{2+} retention capacity (CRC) and matrix Ca^{2+}

Cells are detached with trypsin, centrifuged at 1000 × *g* for 5 min, and washed twice with 1X PBS. The cellular pellet is suspended in KCl medium (130 mM KCl, 10 mM MOPS, 10 μM EGTA, pH 7.4) supplemented with 1 mM EGTA and 200 μM digitonin and incubated for 20 min on ice. Cells are then diluted 1:10 in KCl medium and centrifuged at 1000 x *g* in a refrigerated centrifuge (4 °C) for 5 min. The final pellet is washed in KCl medium and then used for CRC measurements.

To measure the CRC, extra-mitochondrial Ca^{2+} concentration is assessed by measuring Calcium Green-5 N (Cat# C3737 ThermoFisher Scientific, Waltham, MS, USA) fluorescence changes using Victor3^{TM} Plate Reader (PerkinElmer, Waltham, MS, USA) essentially as described [37]. Digitonin-permeabilized HEK293 cells (5×10^6 cells per well, 96-well microplate) are suspended in KCl medium supplemented with 5 mM Succinate, 1 mM Pi, and 0.5 μM Calcium Green-5 N, pH 7.4. For the assay in the presence of rotenone the KCl medium was supplemented with 1 μM rotenone. For all CRC measurements, sequential 5 or 10 μM $CaCl_2$ pulses were added to cells. All measurements are performed in three technical replicates. At the end of the assay, cells are lysed using Extraction Buffer (150 mM NaCl, 20 mM Tris−HCl, 1% Triton, 10% glycerol, 5 mM EDTA, protease inhibitor cocktail, pH 7.4) and protein quantification is performed using Biorad Protein Assay (Cat# 5,000,001 Biorad, Hercules, CA, USA).

To measure matrix [Ca^{2+}] digitonin-permeabilized cells were centrifuged at 1000 x *g*, resuspended in KCl medium supplemented with 100 μM EGTA at 20×10^6 cells/ml and incubated with 3 μM Rhod2-AM for 30 min at room temperature. Permeabilized cells were then washed with KCl medium and resuspended at 10×10^6 cells/ml (2×10^6 cells/well) in KCl medium supplemented with 5 mM succinate and 1 mM Pi. Sequential 5 μM Ca^{2+} pulses were added. To calibrate the Rhod2 signal, a final 1 mM Ca^{2+} bolus and then 10 mM EGTA were added at the end of experiment to measure the maximal and minimal fluorescence, respectively. Total protein was then measured with the BCA method. Matrix [Ca^{2+}] was calculated based on a K_d for Rhod2 of 570 nM.

2.4. Assessment of mitochondrial membrane potential

To determine $\Delta\Psi$m in cells incubated with Tetramethylrhodamine (TMRM) (20 nM) (Cat#I34361; Thermo Fisher Scientific), we used Spinning Disk Confocal microscope (Nikon ECLIPSE Ti, Florence, Italy) with attenuated laser power (around 2%) to minimize the time needed to obtain images and to avoid photobleaching. Next, we started to collected images. Moreover, to compare possible differences in $\Delta\Psi$m between control and SPG7 null cells, all parameters: resolution, laser power, detection gain of a camera and time-lapse interval to obtain images are fixed. Then, TMRM fluorescence intensities was quantified with ImageJ tool and expressed as TMRM intensity/mitochondrial area.

2.5. Visualization and quantification of TMRM flickering events

Our approach allows the measurement of transient changes of mitochondrial membrane potential (m$\Delta\Psi$) that arise from transient opening of the mitochondrial permeability transition pore (mPTP) and can be visualized, as flickers of fluorescence (an example in **SVideo 1** and **SVideo2)**, using Tetramethylrhodamine (TMRM Cat#I34361,Thermo Fisher Scientific, Waltham, MS, USA). TMRM is a rapidly repartitioning cationic, red-orange fluorescent dye that is readily sequestered by polarized mitochondria. Cells are plated on glass bottom dish 35 mm, loaded with 20 nM TMRM, 2 μM Cyclosporine H (CsH) (Cat# SML1575 Sigma-Aldrich, St.Louis, MS, USA) in HBSS + Na_2CO_3 +10 mM Hepes or in complete medium (without phenol red) for 30 min. Under these conditions TMRM operates in non-quenching mode. Then cells are washed and the dish placed on the stage of Spinning Disk Confocal microscope (Nikon ECLIPSE Ti, Florence,Italy) equipped with a stage-top incubator and CO_2 control system.

TMRM flickering was quantified in a stack of time-sequence images (1 s intervals, 300 ms exposure, for a period of about 10 min) acquired with a 60X oil-immersion objective. The “Stack-T function” plugin of ImageJ tool [38] was used to generate a stack of “ΔF,” which is the fluorescence difference between the two images in succession. Therefore, TMRM losses in flickering are shown as black holes in the ΔF image stack. A stack of three-dimensional surface plots was then generated from the ΔF image stack. Peaks in the 3D surface plot in **Fig. 1C** represent the TMRM loss and were counted as flickering events. Stack T-function plugin combined to "Analyze Particles" function (with a thresholding size of 0.7 μm^2) was used to generate an automated macro to detect from each frame in a given time: (i) the total amount of exchanged TMRM fluorescence in a single time interval (total TMRM); (ii) the highest peak per field (max TMRM peaks); (iii) the size of the involved mitochondrial area (flickering area/Total mito area); and (iv) the frequency of events (flickering frequency/Total mito area). Of note, by applying this setting, in the absence of flickering events the macro attributes a 0 value. Frequency and area of TMRM mitochondrial flickering were normalized on total mitochondrial area that is quantified using Mytoe tool [39].

2.6. Constructs generation

For the generation of bicistronic plasmids SPG7-IRES-GFP and SPG7-EQ-IRES-GFP we used In-fusion cloning approach (Takara Bio, Saint Germain en Laye, France). Briefly, plasmids expressing myc-tagged paraplegin (pcDNA3.1-*SPG7*-myc) and paraplegin proteolytic inactive form (pcDNA3.1-*SPG7*-EQ-myc) [9] was linearized with XhoI (New England Biolabs, Ipswich, MS, USA) restriction enzyme and then amplified with the following primers:

Primer fw: 5′-TGAGCCTCGACTGTGCCTTCTAGTT-3′
Primer rev: 5′-CCCAGATCCTCCTCAGAAATCAGC-3′

Plasmid pEGFP-C1 (Addgene, Watertown, MA, USA) was linearized with XhoI (New England Biolabs, Ipswich, MS, USA) restriction enzyme and then GFP region was amplified with the following primers:

Primer fw (containing IRES sequence): 5′-GCTGATTTCTGAGGAG GATCTGGGTGA
CAAACTGTACATGCCGTTAACTGTAATTTTGCGTGATTTTTTTGTA-3′
Primer rev: 5′-AACTAGAAGGCACAGTCGAGGCTCAACTTGTACAGCTCG TCCATGCCG-3′

Then In-fusion cloning protocol was applied according to the manufacturer's instructions (Takara Bio, Saint Germain en Laye, France).

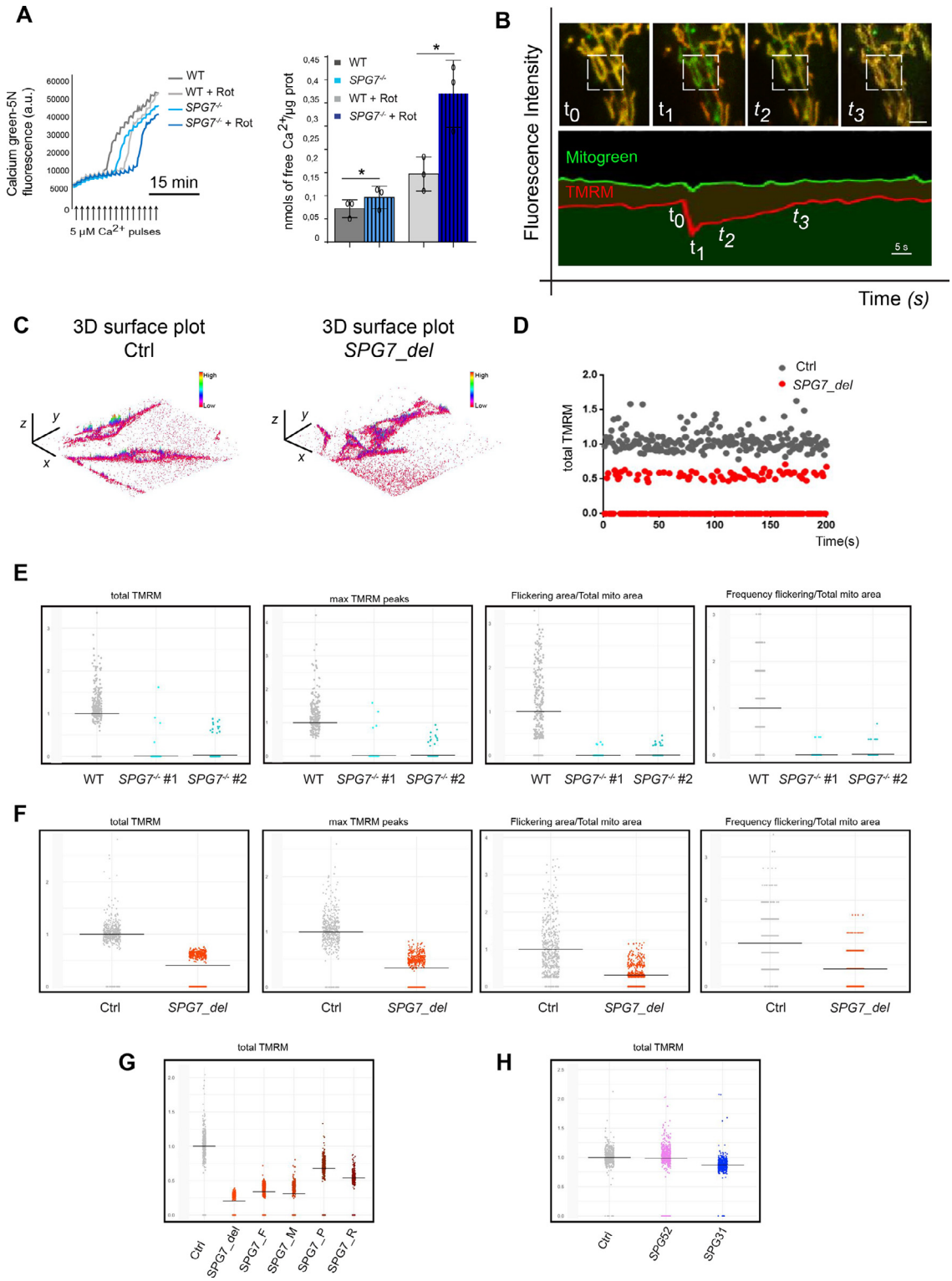

Fig. 1. Mutant paraplegin determines CRC increase and defective flickering.

(**A**) Left, representative traces of mitochondrial uptake of extramitochondrial Ca^{2+} during time monitored by the fluorescence of Calcium Green-5 N given in arbitrary units (a.u.). Arrows indicates sequential Ca^{2+} pulses. Traces from control and *SPG7*$^{-/-}$ HEK293 cells in normal conditions are in dark gray and light blue, respectively, while traces in the presence of rotenone (Rot) are in light gray and dark blue, respectively. Right, bars represent total nmol Ca^{2+}/ug protein uptaken by mitochondria before mPTP opening (data are mean ±SEM, $n = 3$, in three technical replicates, unpaired Student's *t*-test $p < 0.05$). (**B**) Timeframe of a flickering event (inset). TMRM (red) and MitoTracker (green) fluorescence. Bar, 10 μm. (**C**) 3D surface plot of ΔF TMRM flickering signals of two consecutive frames in control and SPG7_del fibroblasts. (**D**) ΔF TMRM flickering signals in 200 s (control, gray; SPG7_del fibroblasts, red). (**E**) Dot plots of four parameters describing the flickering event (total TMRM; max TMRM peaks, Flickering Area/Total mito-area; Frequency of the flickering/Total mito-area) for wild-type (light gray) and *SPG7*$^{-/-}$HEK293 cells (clones #1 and #2, light blue) (three independent experiments, $n > 200$ cells per experiment; Kruskal-Wallis $p < 0.0001$). (**F**) As in E for control (light gray) and *SPG7_del* fibroblasts (orange-red) (three independent experiments, $n > 200$ cells per experiment; Wilcoxon $p < 0.0001$). (**G**) Dot plots of total TMRM for control (light gray), *SPG7_del* and four SPG7 missense mutations fibroblasts (*SPG7_P, SPG7_R, SPG7_M, SPG7_F*; orange-red) (three independent experiments, $n > 200$ cells per experiment; Kruskal-Wallis $p < 0.0001$). (**H**) As in G for control (light gray) and *SPG52* (pink) and *SPG31* (blue) fibroblasts (non-SPG7 HSP) (three independent experiments, $n > 200$ cells per experiment; Kruskal-Wallis p = n.s).

BioID plasmid expressing the paraplegin-biotin ligase fusion protein (p*SPG7*-BirA-HA) has been generated by cloning *SPG7* gene into pcDNA3.1 MCS-BirA(R118G)-HA vector previously described [40] (a gift from Kyle Roux, plasmid #36047, Addgene, Watertown, MA, USA). Forward (Fw AflII: TAAACCTTAAGATGGCCGTGCTGCTGCTGCTG) and reverse (Rev EcoRI: TGAGAATTCCTTGGGCCAAGTCGGCTCTTCG) primers were used to incorporate appropriate restriction sites and eliminate the stop codon in *SPG7* by PCR, starting from the construct pcDNA3.1- *SPG7*-myc [9]. pcDNA3.1 MCS-BirA(R118G)-HA vector and the PCR product of *SPG7* gene were digested by the AflII (Cat# R0520S - New England Biolabs, Ipswich, MS, USA) and the EcoRI (Cat# R3101S - New England Biolabs, Ipswich, MS, USA) restriction enzymes. Ligation between the resulting products were performed by T4 DNA Ligase (Cat# M0202S - New England Biolabs, Ipswich, MS, USA) to generate p*SPG7*-BirA-HA plasmid

2.7. Pharmacological treatments

To confirm the specificity of the mPTP flickering data, control cells were pre-treated with cyclosporin A (CsA; Cat# 59865-13-3 Sigma, St. Louis, Mo, USA) 5 μM for 2 h (data not shown) or with its analog, NIM811 [41], 2 μM for 1 h. CsA (cyclosporin A) and NIM811 (the latter lacking the ability to inhibit calcineurin and therefore devoid of immunosuppressive activity) are widely used to inhibit mPTP opening. Bz-423 [42] (Cat# 5791,Tocris Bioscience, Bristol, UK), an inhibitor of the ATP synthase able to favor mPTP opening by interacting with the OSCP subunit [28], was dissolved in DMSO and used at a final concentration of 100−300 nM. Cells were treated with Bz-423 or vehicle for 1 hour before the starting of the experiments. For the analysis of SIRT3 stability by the cycloheximide (CHX) (Cat# C4859 Sigma-Aldrich, St.Louis, MS, USA) chase assay, cells were incubated with 50 ug/ml CHX for the indicated times. Degradation of the endogenous SIRT3 was monitored by Western blotting using anti-SIRT3. As a negative control, actin protein was used.

2.8. Transient transfection

For HEK293 transfection 70% confluent cell plates (Corning 100 mm, Culture Dish #430,167) were transfected with Lipofectamine 3000 Reagent (Thermo Fisher Scientific, Waltham, MS, USA) according to the manufacturer's instructions. Briefly, for each plate 25 μl of Lipofectamine 3000 were diluted in 1.5 ml of Opti-MEM Medium (Gibco, Thermo Fisher Scientific, Waltham, MS, USA). Separately, master mix was prepared by diluting DNA (12,5 μl [1 μg/μl] /sample) plus P3000™ Reagent (25ul/sample) in 1.5 ml of Opti-MEM Medium. Master mix was then added to diluted Lipofectamine 3000 Reagent (1:1 ratio) and incubated for 15 min at room temperature. DNA-lipid complex was dropped onto plated cells. Cells were incubated at 37 °C and collected 48 h after transfection for subsequent analysis.

For fibroblast transfection 60% confluent cell plates (glass bottom dish 35 mm, Ibidi, Germany) were transfected with Mirus Bio™ TransIT™-LT1 Transfection Reagent (Thermo Fisher Scientific, Waltham, MS, USA) according to the manufacturer's instructions. Briefly, for each plate 1 μl of plasmid (1 μg/ul stock) were diluted in 1.0 ml of Opti-MEM Medium (Gibco, Thermo Fisher Scientific, Waltham, MS, USA). Then 3 μl of Mirus Bio™ TransIT™-LT1 were added to the mix and incubated for 30 min at room temperature. DNA-lipid complex was dropped onto plated cells. Cells were incubated at 37 °C and analyzed 48 h after transfection.

2.9. Immunofluorescence staining

Localization of paraplegin-biotin ligase fusion protein was analyzed by immunofluorescence after 48 h from transfection in fibroblasts cells. Transfected cells were fixed for 10 min in 4% paraformaldehyde (PFA) in PBS, next they were washed three times with PBS and permeabilized with 2.5% BSA + 0.2% Triton X-100 in PBS (blocking buffer) for 45 min. Cells were incubated with anti-HA (Cat# MMS-101P, RRID:AB_2314672, Covance, Princeton, NJ, US) and anti-TIMM23 (Cat# ab116329, RRID:AB_10903878, Abcam, Cambridge, UK) primary antibodies at 4 °C overnight. Cells were then washed three times with PBS and incubated with the appropriate secondary antibodies conjugated to Alexa Fluor 488 (Cat# A-21206, RRID: AB_2535792, Invitrogen, Carlsbad, CA, USA) for 1 h at room temperature. DNA was stained with Hoechst 33342 (Cat# 4082, RRID: AB_10626776, Sigma, St. Louis, Mo, USA). After three washings with PBS, slides were mounted on coverslips with Mowiol (Calbiochem, Darmstadt, Germany) and the images were acquired with confocal fluorescence microscopy (LSM800; Zeiss, Milan, Italy).

2.10. RNAi silencing

To silence SIRT3, equal numbers of cells were transfected using stealth RNAi against the human SIRT3 (Cat# SIRT3HSS118726; Invitrogen, Carlsbad, CA, USA) and stealth RNAi negative control (Invitrogen, Carlsbad, CA, USA) to a final concentration of 100 nM. The transfection reagent was Interferin (Polyplus, Illkirch France) used following manufacturer's instruction. Down-regulation of the target gene was monitored by immunoblot analysis on cell lysates 96 h after transfection.

2.11. BioID assay

Cells were transfected with para-BirA-HA or pBirA-HA vector control (plasmid # 36047, Addgene, Watertown, MA, USA). After 24 h from transfection cell medium was replaced with complete medium containing 50 μM biotin and incubated for 24 h. Mitochondria were isolated and lysed in Lysis Buffer (50 mM TrisHCl pH7.4, 500 mM NaCl, 0,2% SDS, containing protease inhibitor and 10 mM deacetylase inhibitor nicotinamide (NAM)). Affinity purification of biotinylated proteins was performed following protocol's instructions [40]. Briefly, mitochondria lysates were incubated with magnetic streptavidin beads on a rotator at 4 °C overnight. Pulled down biotinylated proteins were then washed three times with different wash buffers (wash buffer #1: 2%SDS; wash buffer #2: 0.1% deoxycholic acid, 1% Triton,1 mM EDTA, 500 mM NaCl, 50 mM HEPES pH 7.5; wash buffer 3: 0.5% deoxycholic acid, 0.5% NP-40, 1 mM EDTA, 250 mM LiCl, 10 mM Tris•Cl pH7.4). Collected biotinylated proteins were resuspended in SDS-PAGE sample buffer (50 mM Tris•Cl pH 6.8, 12% sucrose, 2% SDS, 0.004% bromophenol blue, 20 mM DTT), and their identity was determined by western blot analysis.

2.12. Immunoprecipitation

Five hundred milligrams of mitochondrial extract were lysed from HEK293 cells in RIPA buffer (50 mM Tris−HCl pH 8150 mM NaCl, NP40 1%, 0.5% Sodium deoxycholate, 0.1% SDS, 1 mM EDTA with protease inhibitors (Cat# 539131, Sigma Aldrich, St. Louis, MO, USA) and 10 mM NAM). After a pre-clearing step (incubation of lysate with Protein-A/G−Sepharose beads; Sigma Aldrich, St. Louis, MO, USA) proteins were incubated with anti-acetyl Lysine (Cat# ab190479, Abcam, Cambridge, UK) antibody or normal Rabbit IgG (Cat# 2729, RRID: AB_1031062, Cell Signaling, Beverly, MA, USA) over night at 4 °C with constant gentle agitation. Subsequently, Protein-A/G−Sepharose was added. Precipitates were used for western blot analysis.

2.13. Mitochondria purification

Cells were collected by centrifugation at 600 x *g* for 10 min at 4 °C. The pellet was resuspended in Isolation Buffer (IB) pH 7.4 (0.1 M Tris-MOPS, 0.1 M EGTA/tris, 1 M sucrose, containing protease inhibitor

and 10 mM NAM) and syringed for rapid destruction. The homogenate was centrifuged at 600 x *g* for 10 min at 4 °C. Collected supernatant was re-centrifuged at 7000 x *g* for 10 min at 4 °C. After washing in IB, the pellet containing mitochondria was resuspended in RIPA buffer to extract mitochondrial proteins.

Mitochondria from mice brain were isolated by differential centrifugation. Briefly, brains were minced and homogenized in cold extraction buffer pH 7.2 (125 mM sucrose; 250 mM mannitol; 10 mM HEPES; 10 mM EGTA; 0.01% BSA; 1x protease inhibitors) by using a Dounce homogenizer. The homogenate was centrifugated at 700 x g and 4 °C for 10 min. The pellet containing nuclei and intact cells was discarded and the supernatant was centrifugated again at 700 x g for 10 min at 4 °C and subsequently at 10,000 x g for 15 min at 4 °C. The resulting pellet was resuspended and permeabilized in extraction buffer with digitonin to a final concentration of 0.02%. After a centrifugation at 10,000 x g for 15 min at 4 °C the final pellet was re-suspended in RIPA buffer and protein concentration was determined.

2.14. Western blotting

Mitochondria lysates were prepared in RIPA buffer (50 mM Tris−HCl pH 8,0, 150 mM NaCl, NP40 1%, 0.5% Sodium deoxycholate, 0.1% SDS, 1 mM EDTA with proteinase inhibitors (Sigma Aldrich, St. Louis, MS, USA) and 10 mM NAM (Sigma Aldrich, St.Louis, MS, USA) and sonicated twenty times. Lysates were cleared of insoluble material by centrifugation at 10,000 x *g* at 4 °C and the supernatant was retained for western blotting. Protein extract concentrations were determined using PierceTM BCA Protein Assay Kit (Thermo Fisher Scientific, Waltham, MS, USA) and a spectrophotometer reader (Thermo Fisher Scientific, Waltham, MS, USA) at a wavelength of 595 nm. Protein samples were separated by 4−20% Precast Protein gel (Cat# 4561094 Bio-Rad, Hercules, CA, USA), and transferred to polyvinylidene difluoride (PVDF) membranes (Immobilon-P, Merck Millipore, Darmstadt, Germany) at 110 V for 1.5 h. Membranes were blocked in blocking solution (5%BSA dissolved in TBS-T) and incubated overnight at 4 °C with the commercial primary antibodies: anti-GAPDH 1:10000 (Cat# sc-32233, RRID:AB_627679, Santa Cruz Biotechnology, Heidelberg, Germany); anti-Cyclophilin D 1:1000 (Cat# ab110324, RRID:AB_10864110, Abcam, Cambridge, UK); anti-acetyl Lysine 1:1000 (Cat# ab190479, Abcam, Cambridge, UK); anti-Sirtuin3 1:1000 (Cat# 5490, RRID:AB_10828246, Cell Signaling, Beverly, MA, USA); anti-paraplegin 1:750 (Cat# LS-C175082, LSBio, Seattle, WA, USA); anti HSP60 1:1000 (Cat# SR-806D, RRID:AB_1279011, Enzo Life Sciences, Villeurbanne, France); anti-citrate synthase 1:2000 (Cat# ab96600, RRID:AB_10678258, abcam, Cambridge, UK); anti-catalase 1:1000 (Cat# 12980, RRID:AB_2798079, Cell Signaling, Beverly, MA, USA); anti SOD2 1:750 (Cat# MA1-106, RRID:AB_2536812, Thermo Fisher Scientific, Waltham, MS, USA); anti-HA 1:1000 (Cat# A488−101L-100, RRID:AB_10063991, Covance, Princeton, NJ, US); anti GFAP 1:1000 (Cat# sc-6171, RRID:AB_641023, Santa Cruz Biotechnology, Heidelberg, Germany); anti-IBA1 rabbit polyclonal (1:1000, Cat. No. 234 013; RRID:AB_2,661,873, Synaptic System). For immunodetection of primary antibodies, goat-anti-rabbit-HRP conjugate (Cat# 65−6120, RRID:AB_2533967, GE Healthcare, Chicago, IL, USA) or goat-anti-mouse-HRP conjugate (Cat# 31430, RRID: AB_228307, GE Healthcare, Chicago, IL, USA) was used at 1:5000 in blocking solution, and HRP was detected using Luminata Crescendo chemiluminescence substrate (Cat# WBLUR0500, Millipore, Molsheim, France). Western Blot images were acquired using the Chemi-Doc imaging system (UVP, Cambridge, UK) and densitometric analysis was performed with ImageJ 1.51v software. Signals for each mitochondrial protein staining were quantified and then normalized for citrate synthase (CS) in the same sample. The western blot results shown are representative of at least three independent experiments.

In Fig. 4 and 5 histograms show quantification of indicated mitochondrial proteins normalized by CS (Citrate Synthase), except for Fig. 4C which shows cyclophilin D normalized by immunoglobulin G.

2.15. MitoSox assay

HEK293 cells were incubated for 10 min at 37 °C, protected from light, in Hank's Balanced Salt Solution 1x with calcium and magnesium (HBSS/Ca/Mg) containing 5 μM MitoSOX red fluorogenic dye (Cat# M36008, Invitrogen, Carlsbad, CA, USA). The fluorescence emission was measured through fluorescent activated cell sorter (FACS-BD Accuri C6, Franklin Lakes, NJ, USA) for quantitative recording of mitochondrial ROS levels from individual cells.

2.16. Blue native-polyacrylamide gel electrophoresis (BN-PAGE)

A total of 20 μg of crude mitochondria lysates solubilized in NativePAGE Sample Buffer (Cat# BN2003, Invitrogen, Carlsbad, CA, USA) supplemented with 1% digitonin were loaded onto 3−12% NativePAGE Novex Bis-Tris polyacrylamide gels (Cat# BN1001BOX, Invitrogen, Carlsbad, CA, USA). Following gel electrophoresis, proteins were blotted to PVDF-membranes (Cat# IPVH00010, Immobilon-P, Merck Millipore, Darmstadt, Germany). After transfer, the membranes were blocked with 5% milk in TBS-T. The membranes were incubated overnight with primary antibodies in blocking solution. After washing the membranes three times with TBS-T, HRP-conjugated secondary antibodies were applied for 1 h at room temperature. Detection was performed using Luminata Crescendo (Cat# WBLUR0500, Millipore, Molsheim, France).

2.17. RNA extraction and real time-PCR

Total RNA extracted from cells was isolated by using RNeasy Mini Kit (Cat# 74,106, Qiagen, Hilden, Germany) according manufacturer's instructions. During the extraction protocol, RNAs were digested with DNaseI to remove DNA contaminating. RNA (1 μg) was then reverse transcribed into cDNA by QuantiTect Reverse Transcription Kit (Cat# 205,313, Qiagen, Hilden, Germany) with random hexamers oligo. For quantitative real time PCR analysis (qRT-PCR), cDNAs were analysed with Roche Light Cycler 480 system using a LigthCycler 480 SYBR Green I Master mix (Roche, San Francisco, CA, USA). Quantification data were expressed as cycle threshold (Ct). The Ct values were averaged for each in-plate technical triplicate. The averaged Ct was normalized as difference in Ct values (ΔCt) between each sample and the GAPDH gene, used as endogenous reference. The ΔCt values were normalized with respect to the ΔCt values of the control ($\Delta\Delta$Ct). The variation was reported as fold change (2 -$\Delta\Delta$Ct). All the results are shown as means ± SEM.

Human SIRT3 primers used for Real Time PCR:

Fw 5′-GCATTCCAGACTTCAGATCGC-3′
Rev 5′-GCAGCCGGAGAAAGTAGTGA-3′

2.18. Neuronal cultures

Primary cultures were prepared from P0-P2 *Spg7*$^{+/-}$ and *Spg7*$^{-/-}$ mice, following standard procedures [43]; [44], with some modifications. In brief, extracted cerebral cortices (excluding hippocampus) were cut into 1 mm^3 pieces, and treated with trypsin (0.15%) and DNAse (10 μg/ml), for 30 min at 37 °C with gentle shaking. Next, cells were mechanically dissociated and plated on dishes pre-coated with polyethyleneimine 0.1% (wt/vol). For MEA experiments, cells were plated at a density of 1200−1500 × 10^3 cells/ml. For patch-clamp experiments, cells were plated on 35 mm culture dishes, at a density of 600−750 × 10^3 cells/ml. After 3 h, the plating medium was

replaced with neurobasal medium supplemented with B27 (Invitrogen, S. Giuliano Milanese, Italy), 1 mM glutamine, and bFGF (10 ng/ml). MEA cultures were covered with gas-permeable covers (MEA-MEM; Ala-Scientific Instruments, Inc., Farmingdale, NY) throughout the culture period, and maintained at 37 °C, in 5% CO2. One-half of the medium volume was replaced every three days. In a fraction of dishes, network activity was monitored by MEA between 12 and 24 days in vitro (DIV).

2.19. MEA recording and burst analysis

We used MEA dishes with 60 ITO electrodes (30 μm diameter) spaced 200 μm apart (Multichannels System, Germany). Registrations were carried out at 36 °C, in CO_2-controlled incubators, on MEA dishes usually presenting at least 50 active electrodes. The rare units that fired continuously were discarded. Data were acquired as previously reported [45]· [46] during 2 h continuous recording, at the indicated DIV. In brief, signals were sampled at 40 kHz with MEA-1060BC or 1060INV pre-amplifiers (bandwidth 1−8000 Hz, Multichannel Systems), connected to a MEA workstation (bandwidth 100−8000 Hz, Plexon Inc., Dallas, TX, USA). Data were sorted into timestamp files by using the MEAWS software and artifacts cleaned with the OFFLine Sorter software (Plexon Inc., Dallas, TX, USA). Action potential bursts were identified with Neuroexplorer. A burst was defined by using the following parameters: minimum number of spikes: 2; minimum duration: 3 ms; minimum interval between bursts: 0.9 s; maximum inter-spike interval of 0.2 s, to define start of burst, and 0.3 s, to define end of burst. In Fig. 3A, data are representative of analogous experiments carried out on 13 MEA chambers, from 4 *Spg7*$^{+/-}$ and 3 *Spg7*$^{-/-}$ mice, between 13 DIV and 16 DIV. In **Figure S4A**, the results obtained from 3 recording chambers were pooled for each mouse. A total of 71,925 individual bursts from 3 h 45′ recording were analyzed for *Spg7*$^{+/-}$, and 50,177 bursts from 4 h 17′ for *Spg7*$^{-/-}$.

2.20. Fluorescent measurement of synaptic activity using FMDye1-43 in dissociated cortical cultured neurons

Recycling of synaptic vesicles are essential for neurotransmission. To gain mechanistic understanding of these processes, we did direct measurements of vesicle release and retrieval by FM1−43 styryl dye (Cat# T3163 Thermo Fisher Scientific, Waltham, MS, USA) since their loading and unloading are reliable measurements for synaptic vesicle release and retrieval in cultured neurons. The imaging procedures that we used have been previously described [47]· [48]. Briefly, presynaptic terminals were labeled by exposure to styryl dye (10 μM FM1−43) during high-K^+ depolarization (modified Tyrode, 55 mM KCl).

Dye was kept in the extracellular solution for 1 min to let the nerve terminal recover in the presence of the dye and allow for complete endocytosis of all released vesicles. Then, the extracellular FM dye was washed away by replacing the solution multiple times with fresh saline solution. All staining and washing protocols were performed with modified Tyrode containing 10 μM NBQX and 20 μM D-AP5 to prevent dye loss due to spontaneous neuronal activity. Images were taken after 10- to 15-min washes in dye-free solution. The amount of fluorescence in each terminal was quantified using ImageJ analysis software. We analyzed around 300 synaptic boutons from both *Spg7*$^{+/-}$ and *Spg7*$^{-/-}$neurons treated with Bz-423 or vehicle between 13 DIV and 16 DIV. Upon fluorescence quantification, data were displayed as mean ±SD. One-way ANOVA followed by the Tukey-Kramer method was used for comparing groups. To image vesicle release, synaptic vesicle exocytosis was stimulated with the depolarizing solution (modified Tyrode, 55 mM KCl) during the imaging process. As vesicles exocytosed, dye was released into extracellular space and was quickly washed away. The amount of fluorescence in each synaptic bouton was quantified for each time point using ImageJ analysis software. Loss in fluorescence measured during stimulation (expressed as percentage of fluorescence intensity at the time of stimulation; T0: 100% fluorescence) indicates the rate of synaptic vesicle exocytosis and is calculated as (F - Fmin)/(Fmax - Fmin), in which Fmax is the average of the first 3 frames at a baseline before stimulation, and Fmin is the average of the last 3 frames after high K^+ stimulation. All fluorescence intensity values are background subtracted. Values were displayed as fluorescence traces. RM one-way ANOVA followed by the Tukey-Kramer method was used for comparing groups.

2.21. Whole-cell patch-clamp recording

Experiments were carried out at room temperature, during the third week in culture,to minimize the variability caused by network maturation[44]. For stimulation and recording, we used an Axopatch 200B amplifier (Molecular Devices, Sunnyvale, CA, USA). Cell capacitance and series resistance were always compensated (up to approximately 75%), and monitored during recording. Access resistance (R_a) was usually below 35 MΩ. Cells in which the initial R_a was ≥ 40, or R_a changed more than 20% during the experiment were discarded. Currents were low-pass-filtered at 2 kHz and acquired online at 5 to 10 kHz with pClamp 9 hardware and software (Molecular Devices, Sunnyvale, CA, USA). To study spontaneous and miniature EPSCs, cells were perfused with an extracellular solution containing (mM): NaCl 130, KCl 5, $CaCl_2$ 2, $MgCl_2$ 2, HEPES 10, and D-glucose 5 (pH 7.3). Borosilicate micropipettes (3−5 MΩ) contained (mM): K-gluconate 140, KCl 5, $MgCl_2$ 1, BAPTA-KOH 0.5, HEPES 10, NaGTP 0.3 and MgATP 2 (pH 7.3). A physiological $[K^+]_i$ allowed us to recognize regular spiking pyramidal neurons, before studying the synaptic events. Action potentials were characterized as reported [49]. To isolate miniature EPSCs, 1 μM TTX was added to the extracellular solution. Bath solution and drugs were applied with an RSC-160 Rapid Solution Changer (Bio-Logic Science Instruments, Seyssinet-Pariset, France). When testing Bz-423 (300 nM), cells were pretreated for one hour before recording.

2.22. Electrophysiology data analysis

Spontaneous EPSCs and mEPSCs were recorded as inward events at −68 mV (i.e. close to the reversal potential for GABAergic currents). Synaptic events were analyzed with Mini Analysis Program (Synaptosoft, Fort Lee, NJ, USA) and OriginPro 2018 (OriginLab, Northampton, MA, USA). Spontaneous synaptic events comprised smoothly shaped isolated as well as composite signals. EPSCs were inspected one by one, to exclude spurious events. The baseline noise (peak to peak) was generally ~7 pA. The threshold was usually set at 5−6 pA. In each cell, the distribution of EPSC amplitudes and interevent intervals was analyzed with the Kolmogorov-Smirnov (KS) test, on at least 5 min continuous recording (usually containing several hundred synaptic events). The KS test was also applied to compare the inter-burst interval (IBI) distributions obtained from MEA data, in **Figure S4A**. The results of multiple experiments are given as mean values ± SEM, or medians. Unless otherwise indicated, n indicates the number of tested mice. Statistical comparisons between two populations of data were carried out with paired or unpaired Student's *t*-test, after testing the data were normally distributed (with the Shapiro-Wilk test), with homogeneous variances (with F-test). The Welch correction was applied in case of non-equal variances. The Mann-Whitney test was used in case of non-normal distributions. Multiple comparisons were carried out with one-way ANOVA with Tukey-Kramer post-hoc pairwise comparisons (for normally distributed data), or the Kruskal-Wallis test (for non-normal distributions, i.e. **Fig. 3E and S4B**). In **Fig. 3E**, we used the Fisher's exact test to compare the fraction of neurons displaying the different behaviors. The level of statistical significance was generally set at $p < 0.05$, and indicated as *.

2.23. Chemicals and drugs

Unless otherwise indicated, chemicals were purchased from Sigma-Aldrich. Stock solutions of TTX (Tocris, Bristol, UK; 1 mM) were prepared in distilled water and stored at −20 °C. Stock solutions (10 mM) of 4-AP were prepared weekly in our extracellular solution and kept refrigerated. Bz-423 (Tocris Bioscience, Bristol, UK) (5 mM) is dissolved in DMSO and kept refrigerated. The final concentrations were prepared daily in our extracellular solution.

2.24. Animals

In this study we utilized *Spg7* mouse line (*Spg7*$^{-/-}$), a model generated and described in detail in [5]. WT mice were obtained from the Charles River Laboratories to maintain the employed line on a C57BL/6J background.

In all experiments we used as control aged-matched littermates of Spg7$^{+/-}$ mice. Mice were housed in groups of up to five animals/cage under 12-hr light/dark cycles, with ad libitum access to vivarium chow and water. Assignment of animals to treatment groups was conducted in a random manner and was balanced for sex, and researchers were blinded to genotype and treatment groups during behavioral test and analysis of histological data.

2.25. Mice treatment

Spg7$^{-/-}$ and age-matched *Spg7*$^{+/-}$ mice, starting from four months of age, have been treated with either intraperitoneal injection at a single dose of Bz-423 (60 mg/kg/day) in a volume of 100 μl saline or with the respective vehicle (DMSO/saline) in which the Bz-423 was suspended, three times weekly, until six or ten months of age, and then tested for Rotarod performance.

2.26. Rotarod analysis

Motor performance was evaluated with Rota-Rod apparatus (accelerating model; Ugo Basile, Varese, Italy).Female and male mice were housed in plexiglass cages (18 × 35 × 12 cm) with free access to food and water and kept at a temperature range between 20 and 23 °C. All tests were carried out in a behavioral testing room maintained under constant light, temperature, and humidity. The mice were tested during daylight hours (between 9 AM and 6 PM). Before testing, animals were habituated to the testing room for at least 30 min. Groups of *Spg7*$^{-/-}$ and age-matched heterozygous mice were analyzed at 6 or 10 months of age after treatment with Bz-423 (60 mg/die/kg) or vehicle. Before the first test, mice were trained on the rotarod for 60 s at 4 rpm at constant speed. For the tests, mice were placed on the accelerating rod at a starting speed of 4 rpm, reaching a final speed of 40 rpm in 5 min. Mice were tested for four trials per day for three consecutive days. The animals were allowed to stay on the rod for a maximum of 500 s and the time of hold on the rod was scored. For Rotarod experiment we have considered together both male and female mice since we didn't find any sex differences in spatial task performance. We confirmed that *Spg7*$^{-/-}$ mice develop normally with weight comparable to control littermates at six months of age [5], and found that Bz-423 administration didn't cause any statistically significant loss of body weight (data not shown). All behavioral tests were performed by the same experimenter blinded to genotype.

2.27. Immunolabeling

Medial sagittal sections of frozen brain tissue were cut on a cryostat at 12 mm of thickness, fixed with 4% PFA, permeabilized (PBS, 0.2% Tween-20, and 10% fetal bovine serum), and stained with anti-GFAP rabbit polyclonal (1:500, Cat# Z033429−2; RRID: AB_10,013,382; Agilent Technologies) or anti-IBA1 rabbit polyclonal (1:500, Cat. No. 234 013; RRID:AB_2,661,873, Synaptic System). After overnight incubation with primary antibody, sections were washed in PBS 1 × and incubated with Alexa Fluor 594-conjugated donkey anti-rabbit (1:500; Molecular Probes Invitrogen Cat# A-2120; RRID: AB_141,637, now part of Thermo Fisher). Rinsed sections were mounted with VECTASHIELD mounting medium with 4′,6-diamidino-2-phenylindole, dihydrochloride (DAPI) (Vinci-Biochem, Florence, Italy) and analyzed by epi-fluorescent using Leica DM5500 Scanner microscopy.

2.28. Detection of apoptotic cells

The number of apoptotic cells was analyzed by TdT-mediated dUTP nick end labeling (TUNEL), using the In Situ Cell Death Detection Kit, Fluorescein (Roche Cat# 11,684,795,910) following the manufacturer's directions. Twelve-micrometer cryosections were collected on slides and submit to TUNEL assay. To consider the presence of unspecific results, some brain sections were incubated with the reaction mix without TUNEL reaction enzyme. Sections were observed with a Leica DM-6000 microscope and then confocal images were acquired using the LSM710 Zeiss Confocal Microscopy system. The number of TUNEL-positive cells was evaluated by manual counts in brain regions with positive staining.

2.29. Transmission electron microscopy of spinal cord

Following deep anesthesia mice were subjected to transcardial perfusion with Phosphate Buffer Saline (PBS 1X) and spinal cord was harvested by hydraulic extrusion [50] and fixed with 4% paraformaldehyde/2% glutaraldehyde in 0.1 M phosphate buffered saline, pH = 7.4. The lumbar tract of the spinal cord was surgically dissected and kept overnight at 4 °C in the same fixing solution and post-fixed in 1% osmium tetroxide, dehydrated, and embedded in resin. Ultrathin sections taken from the selected regions were cut on ultramicrotome LEICA EM UC7, and the morphology of cellular and subcellular structures was analyzed. In particular, the mitochondrial swelling in lumbar tract axons was evaluated by counting approximately 160 axons per mouse.

2.30. Statistics

TMRM flickering data generated by ImageJ tool from each experiment are normalized respect to control cell samples and are reported as distributions with mean line (as in Dot Plot in **Figs. 1**,**2** and **Supplementary Figures 1,2,3**) and as mean ± SEM (as in Box plot in **Fig. 2**) (n = 3 independent experiments). Statistical significance was assessed using non-parametric tests for the comparison of data samples. We used Wilcoxon rank sum test to compare two independent groups of samples (as in **Figs. 1F and 2A**). A p-value less than the significance level 0.05 was considered statistically significant. Kruskal-Wallis test by rank was performed when there are more than two groups (as in **Figs. 1E**,**1G**,**1H, 2B and 2D**). A p-value less than the significance level 0.05 was considered statistically significant. In this last case, pairwise test for multiple comparisons of mean rank sums (Nemenyi-test as in **Fig. 2B and 2D**) (multiple pairwise tests against all groups) or Pairwise Test for Multiple Comparisons of Mean Rank Sums with one control (Dunn's-Test as in **Fig. 1E**,**1G and 1H**) (multiple pairwise tests against a reference group) were applied to test which pairs of samples are different. A p-value less than the significance level 0.05 was considered statistically significant. All the statistical analyses were carried out in the R environment. The Dot-plots (as in **Figs. 1, 2 and Supplementary Figure 1,2,3**) and the Bar-plots (as in **Fig. 2**) were generated by using ggplot2 and ggpubr R packages.

For CRC experiments (in **Fig. 1A**) data are expressed as mean ± SEM (n = 5 independent experiments); A Two tailed Student's t-test

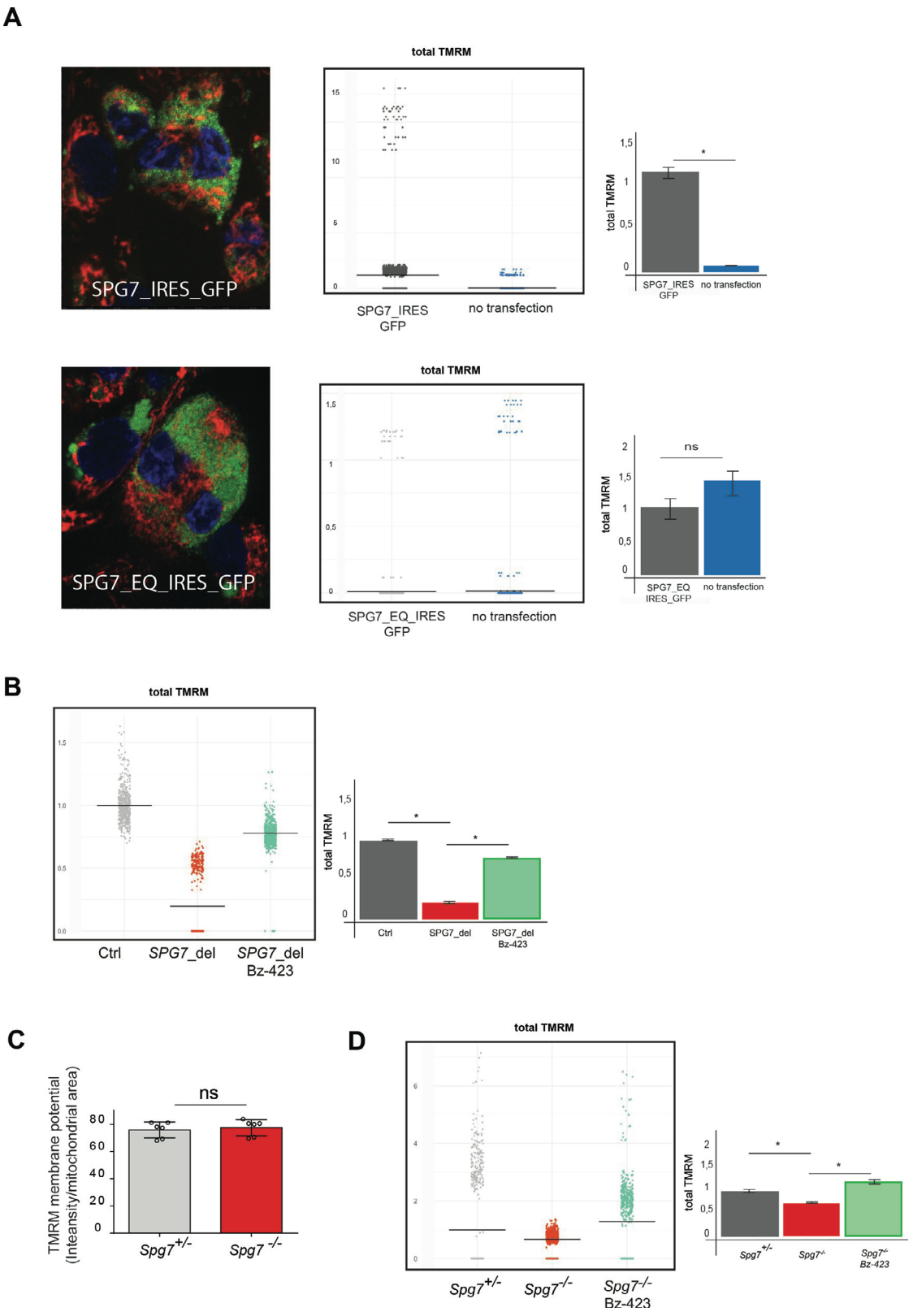

Fig. 2. Genetic and pharmacologic rescue of SPG7 dysfunctional flickering.

(**A**) *SPG7_del* fibroblasts transfected with SPG7_IRES-GFP (upper panel) or SPG7_EQ_IRES_GFP (the proteolytically inactive form; lower panel) constructs (TMRM, red; GFP, green; blue, DAPI). Total TMRM as dot and bar plots are shown for transfected (gray) and untransfected (blue) cells (three independent experiments, n = 46 cells SPG7_IRES-GFP, n = 23 cells SPG7_EQ_IRES_GFP; Wilcoxon $p < 0.0001$) no transf =untransfected. (**B**) total TMRM as dot and bar plots of control (gray), *SPG7_del* (red), and Bz-423 treated *SPG7_del* fibroblasts (green) (three independent experiments, $n > 200$ cells per experiment; Kruskal-Wallis $p < 0.0001$). (**C**) Membrane potential is unchanged in $Spg7^{+/-}$ (gray) and $Spg7^{-/-}$(red) cortical neurons (three independent experiments, n = 6 mice/group; unpaired Student's t-test p=ns) A.U.=arbitrary unit. (**D**) As in **B** on cortical neurons from $Spg7^{+/-}$ (gray), $Spg7^{-/-}$ (red), and Bz-423 treated $Spg7^{-/-}$ (green). (three independent experiments,n = 6 mice/group; Kruskal-Wallis $p < 0.0001$).

Bar plot are expressed as mean ±SEM.

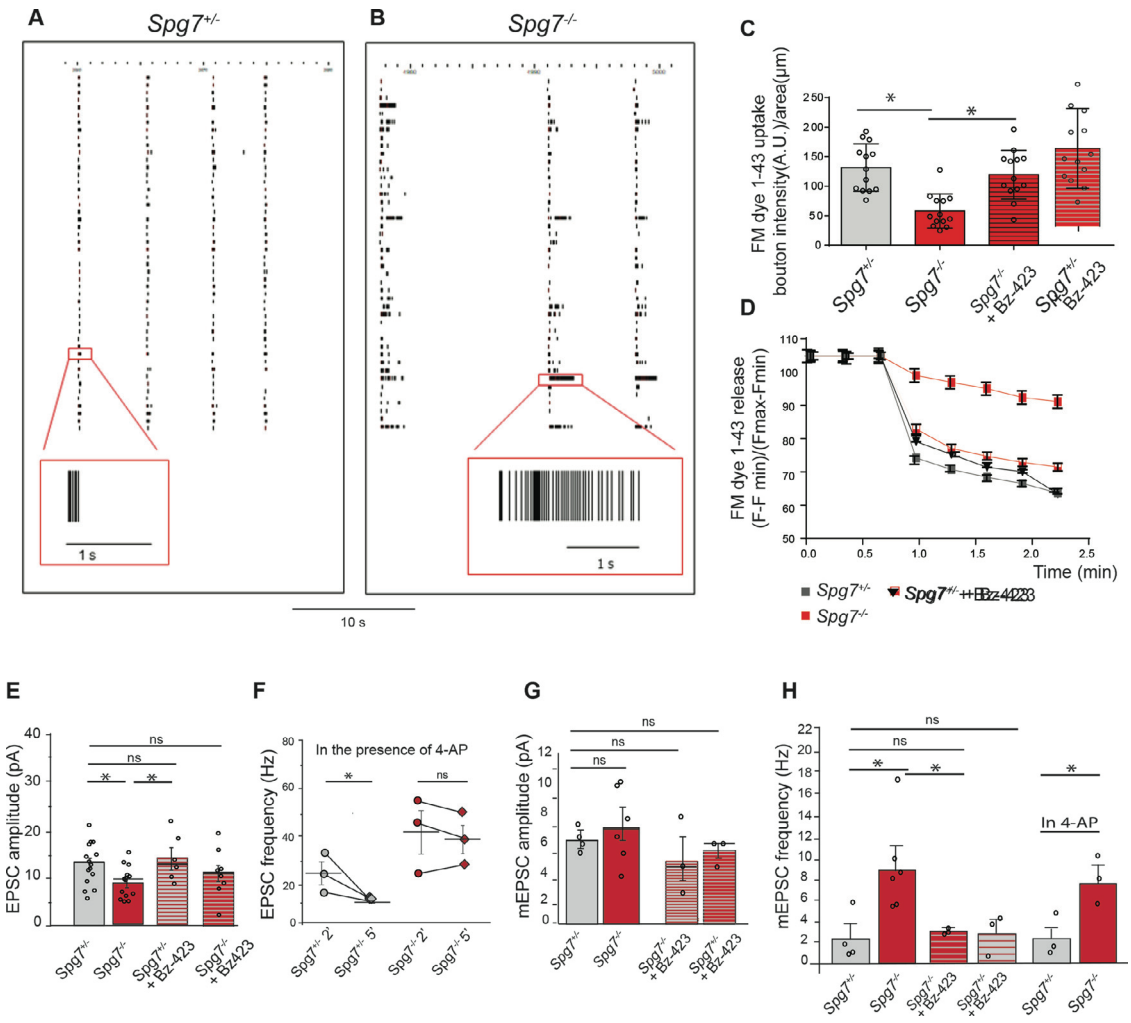

Fig. 3. Deleting SPG7 alters the activity pattern in neocortical cultures and Bz-423 treatment restores synaptic transmission.

(**A**) Raster plot of *Spg7*$^{+/-}$ neurons' firing recorded with MEAs. Vertical ticks are timestamps representing single spikes. Each row shows the trace recorded by one electrode. The columns of quasi-simultaneous spike series in different rows represent network bursts. Inset: an action potential burst from a single unit. (**B**) Same as (**A**), for *Spg7*$^{-/-}$neurons. (**C**) Synaptic terminal endocytosis of *Spg7*$^{+/-}$(Ctrl), *Spg7*$^{-/-}$ treated or not with Bz-423 in cortical neurons by FM1−43 dye uptake;(three independent experiments, n = 6/group, one-way ANOVA $p<0.05$). (**D**) Synaptic vesicles release (exocytosis,three independent experiments, n = 6/group, RM one-way ANOVA $p<0.05$). (**E**) Average of the median EPSC amplitudes in *Spg7*$^{+/-}$(13 ± 0.91 pA; n = 17 neurons), *Spg7*$^{-/-}$ (8.7 ± 0.74 pA; n = 15 neurons; one-way ANOVA p = 0.018 compared to *Spg7*$^{+/-}$), *Spg7*$^{+/-}$+ Bz-423 (14 ± 2.1 pA; n = 5; one-way ANOVA p = 0.04 compared to *Spg7*$^{-/-}$), *Spg7*$^{-/-}$+ Bz-423 (11.1 ± 1.6; NS compared to *Spg7*$^{+/-}$). (**F**) Average EPSC frequencies (Hz) at the 2nd and 5th min in the presence of 4-AP, in *Spg7*$^{+/-}$ (p = 0.023; paired t-test) and *Spg7*$^{-/-}$ neurons (p = 0.927; paired t-test; n = 3 mice/group). (**G**) Average of the median mEPSC amplitudes in *Spg7*$^{+/-}$ (7.2 ± 0.4 pA), *Spg7*$^{-/-}$ (8.2 ± 0.96 pA), *Spg7*$^{+/-}$ + Bz-423 (5.8 ± 1.48 pA), *Spg7*$^{-/-}$ + Bz-423 (6.2 ± 0.5 pA). These values are ns (Kruskal-Wallis; n = 3–6 mice/group). (**H**) Average mEPSC frequency in *Spg7*$^{+/-}$ (2.5 ± 1.25 Hz), Spg7$^{-/-}$ (9.75 ± 1.7 Hz), *Spg7*$^{-/-}$+ Bz-423 (3.3 ± 0.18 Hz), *Spg7*$^{+/-}$ + Bz-423 (3.1 ± 1.2 Hz). *Spg7*$^{-/-}$vs *Spg7*$^{+/-}$$p$ = 0.016; *Spg7*$^{+/-}$ vs *Spg7*$^{+/-}$ + Bz-423 ns; *Spg7*$^{+/-}$ vs *Spg7*$^{-/-}$+ Bz-423 ns; *Spg7*$^{-/-}$ vs *Spg7*$^{-/-}$+ Bz-423 (one-way ANOVA p = 0.04; n = 3–6 mice/group; 23 neurons were overall tested for *Spg7*$^{+/-}$ and *Spg7*$^{-/-}$); ns = not significant. In the presence of 4-AP: *Spg7*$^{+/-}$ (2.4 ± 1.06 Hz) and Spg7$^{-/-}$ (7.93 ± 1.25 Hz), unpaired t-test p = 0.028 (n = 3 mice/group; 17 neurons).

was used for comparing groups. A p-value less than the significance level 0.05 was considered statistically significant.

For TMRM membrane potential experiments (as **in Fig. 2C**) data are reported as mean ± SD. Two tailed Student's t-test was used for comparing groups (*Spg7*$^{+/-}$ vs *Spg7*$^{-/-}$ = not significant). For matrix [Ca^{2+}] determinations (in **Figure S1C)** the two-way ANOVA test (with Bonferroni correction) was performed after extrapolation to identical Ca^{2+} loading values.

For synaptic vesicles recycling experiments and quantification of swollen mitochondria (FM-dye uptake as in **Fig. 3C and Figure S7H**) data were displayed as mean ±SEM. One-way ANOVA followed by the Tukey-Kramer method was used for comparing groups. In synaptic vesicles release experiment (FM-dye release as in **Fig. 3D**) One-way ANOVA with repeated measurements followed by the Tukey-Kramer method was used for comparing groups. A p-value less than the significance level 0.05 was considered statistically significant.

For Rotarod test (**Fig. 7A and B, Figure S6A**) One-way ANOVA with repeated measurements followed by the Tukey-Kramer method was used for comparing groups. A p-value less than the significance level 0.05 was considered statistically significant.

For western blot and real time experiments, quantitative data are reported as the mean ± SEM (Standard Error of the Mean). Two tailed Student's t-test and one-way ANOVA with repeated measurements were applied, when appropriate, to determine statistical significance of the differences. The ANOVA test assumes that, the data are normally distributed and the variance across groups are homogeneous. We can check that with the following tests:

- Levene's test was used to check the homogeneity of variances (i.e., the assumption of equal variances for all groups). If the p − value is greater than the significance level of 0.05, than we can assume the homogeneity of variances in the different treatment groups.

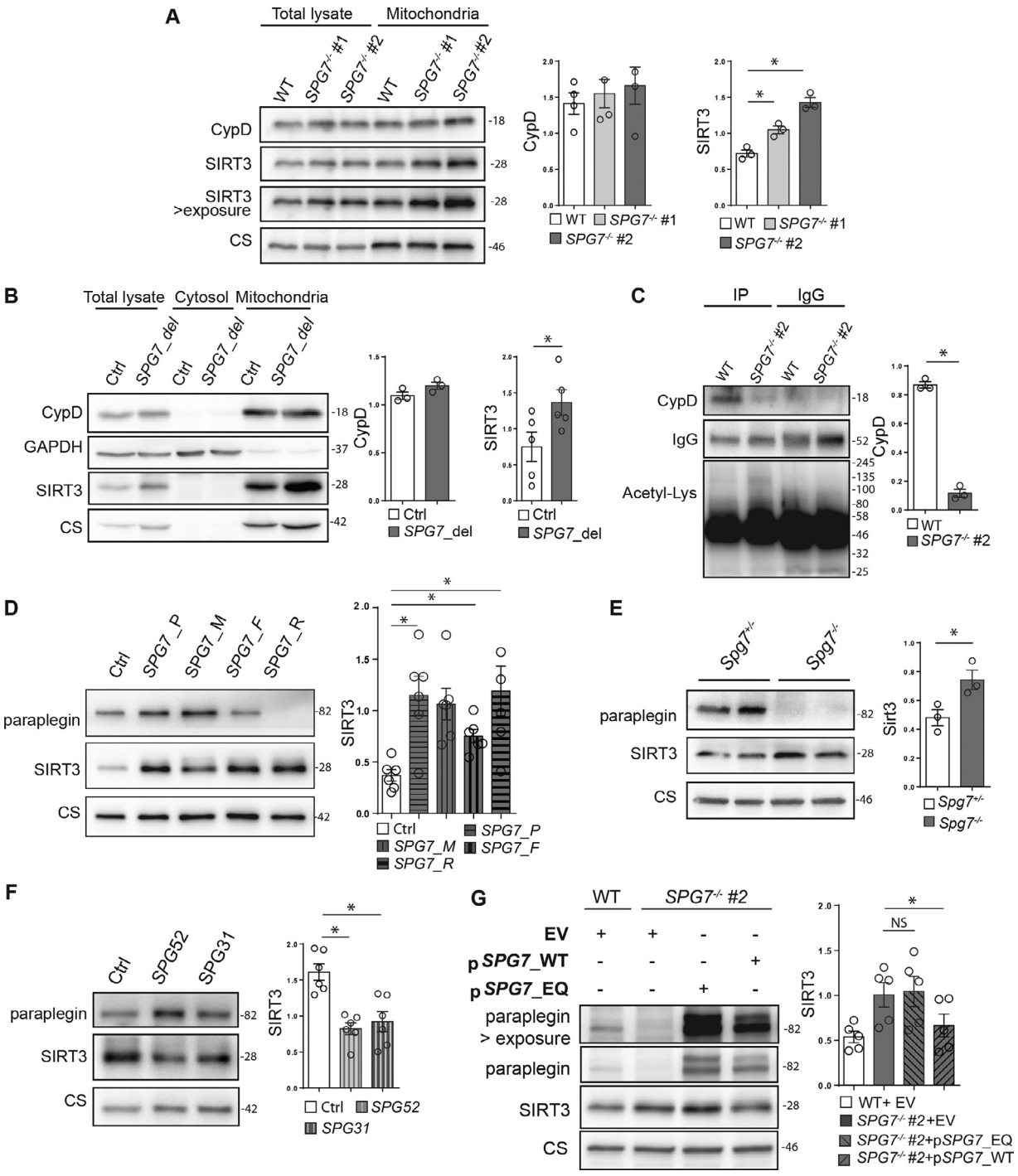

Fig. 4. Protease activity of paraplegin regulates SIRT3.

(**A**) CypD and SIRT3 western blot of total and mitochondrial lysates of WT and *SPG7*$^{-/-}$ #1 and #2 HEK293 clones ($n = 4$, CypD; $n = 3$, SIRT3; one-way ANOVA $^{*}p < 0.05$). (**B**) CypD and SIRT3 western blot of total, cytosolic and mitochondrial fractions of human control (Ctrl) and *SPG7*_del fibroblasts ($n = 3$ independent experiments, CypD; $n = 5$ independent experiments, SIRT3; paired Student's *t*-test $^{*}p < 0.05$). (**C**) Anti-acetyl lysine immunoprecipitation of mitochondrial fractions from WT and *SPG7*$^{-/-}$ #2 HEK293 cells revealed by WB for CypD ($n = 3$ independent experiments; paired Student's *t*-test $^{*}p < 0.05$). (**D-F**) SIRT3 WB of human fibroblasts from SPG7 patients carrying missense mutations (*SPG7*_P; *SPG7*_M; *SPG7*_F; *SPG7*_R; mitochondrial fractions) ($n = 6$ independent experiments; one-way ANOVA $^{*}p < 0.05$)(**D**); cortical neurons of *Spg7*$^{+/-}$ and *Spg7*$^{-/-}$ mice ($n = 3$ independent experiments; $n = 2$/group; unpaired Student's *t*-test $^{*}p < 0.05$) (**E**); non-*SPG7* HSP (*SPG52* and *SPG31*, mitochondrial fractions) ($n = 6$ independent experiments; one-way ANOVA $^{*}p < 0.05$) (**F**). (**G**) SIRT3 WB of mitochondrial fractions of *SPG7*$^{-/-}$#2 HEK293 cells transfected with wild-type paraplegin (p*SPG7*_WT), the proteolytic-inactive (p*SPG7*_EQ), or empty vector (EV) constructs ($n = 5$ independent experiments; one-way ANOVA $^{*}p < 0.05$). Data are expressed as mean ±SEM.

- Shapiro-Wilk test on the ANOVA residuals was applied to verify that the residuals are normally distributed. The $p - \text{value} > 0.05$ indicates that normality is not violated.

As the p-value is less than the significance level 0.05, we can conclude that there are significant differences between the groups in the model summary.

As the ANOVA test is significant, we can compute Tukey Honest Significant Differences for performing multiple pairwise-comparison between the means of groups.

The Welch one-way test was used when the assumption of equal variances for all groups is violated. As the p-value is less than the significance level 0.05, pairwise comparisons between group levels with corrections for multiple testing was calculated.

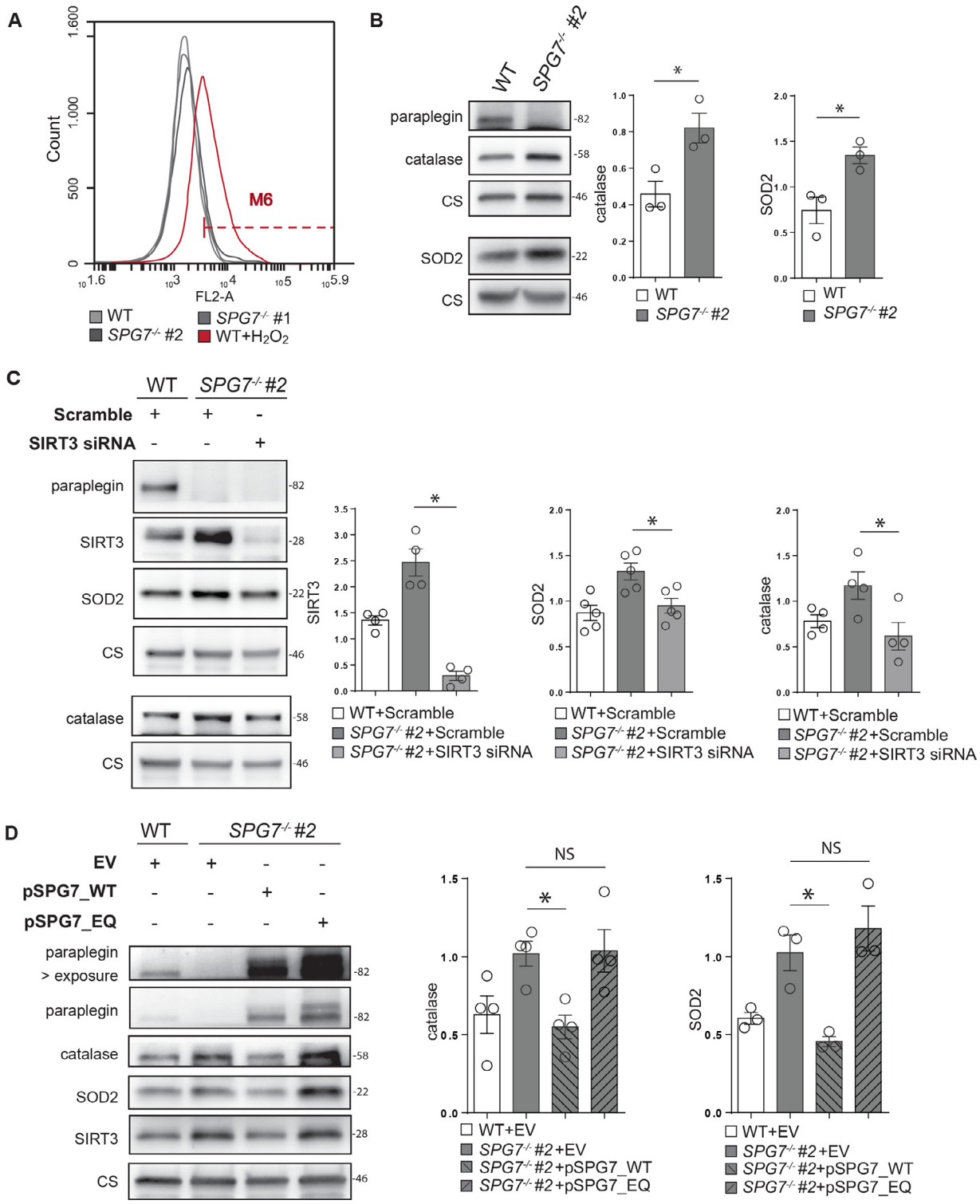

Fig. 5. Paraplegin loss increases antioxidant defense response.

(**A**) MitoSOX-based FACS assay of WT (light gray), *SPG7*$^{-/-}$ #1, *SPG7*$^{-/-}$ #2 (dark gray lines) and H_2O_2-treated WT HEK293 cells (positive control; red). (n = 30,000 cells/sample). (**B-D**) SOD2 and catalase WB of mitochondrial fractions of WT and *SPG7*$^{-/-}$ #2 HEK293 cells (n = 3 independent experiments; paired Student's t-test *$p < 0.05$) (**B**), *SPG7*$^{-/-}$ #2 HEK293 cells transfected with scramble siRNA or *SIRT3* siRNA (n = 4 independent experiments, SIRT3; n = 5 independent experiments, SOD2; n = 4 independent experiments, catalase; one-way ANOVA *$p < 0.05$) (**C**), and p*SPG7*_WT, the proteolytic-inactive p*SPG7*_EQ, or empty vector (EV) constructs (n = 3 independent experiments, SOD2; n = 4 independent experiments, catalase; one-way ANOVA *$p < 0.05$) (**D**). Data are expressed as mean ±SEM.

In Fig. 6E a statistical modeling approach was performed based on Gaussian processes, as described by Kalaitzis and Lawrence [51]. A statistical modeling approach was applied based on Gaussian processes to test the statistical difference between control fibroblast (blu line) and SPG7_del (red line). The statistical significance value llr of the difference in CHX measured for SIRT3 in control and in SIRT3 in SPG7_del was computed (llr=6.899). The statistical significance is indicated by asterisk (llr>0).

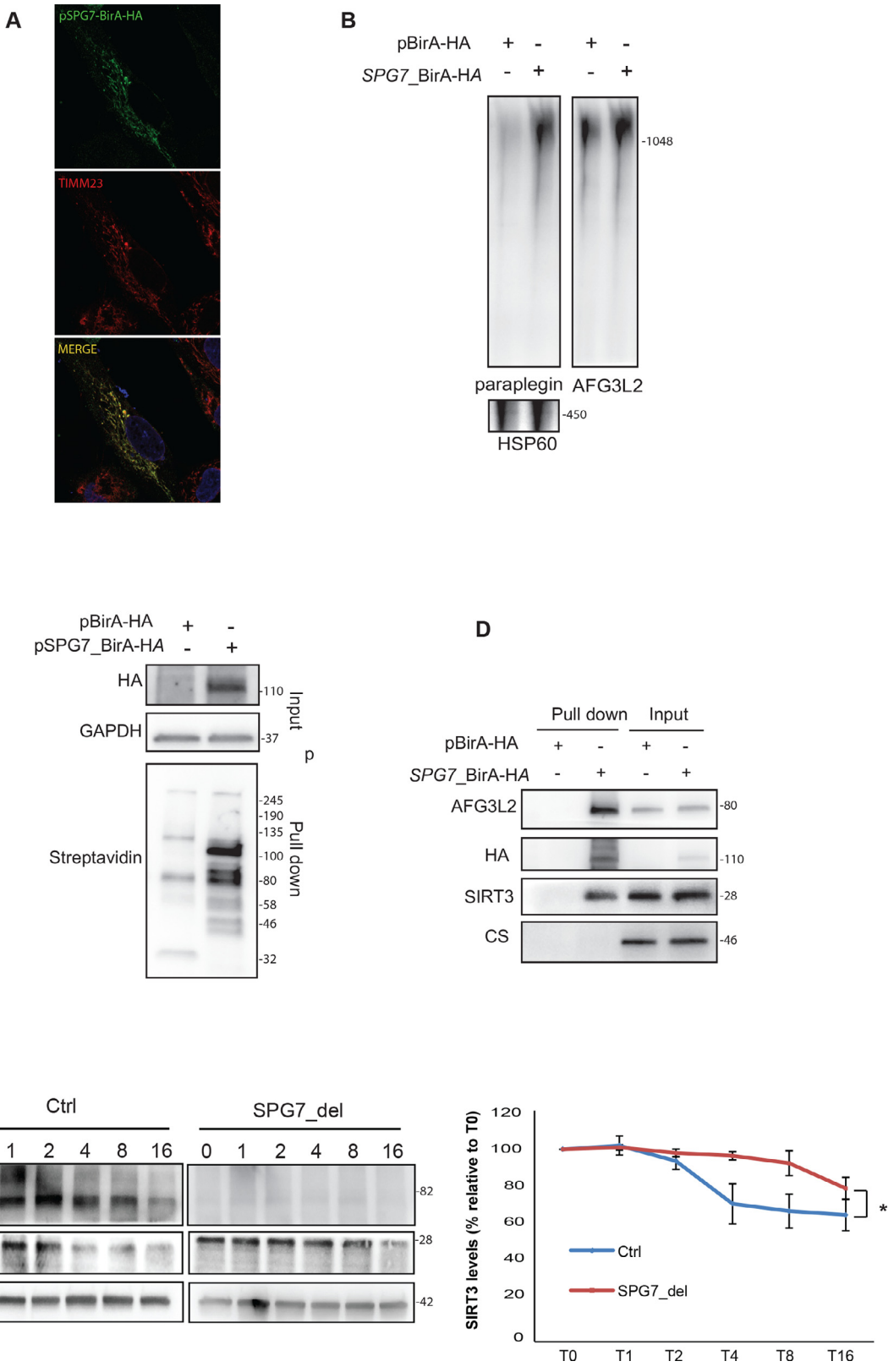

Fig. 6. Paraplegin interacts with SIRT3.

(**A**) Mitochondrial staining of TIMM23 (red) and paraplegin-BirA (green) in human fibroblasts transfected with pSPG7-BirA-HA. (**B**) BN-PAGE of *SPG7*$^{-/-}$ #2 HEK293 cell transfected with pBirA-HA or pSPG7-BirA-HA. (**C**) Immunoblot analysis of SPG7$^{-/-}$ #2 HEK293 cell transfected with control (pBirA) or pSPG7-BirA-HA constructs. Streptavidin-HRP was used to visualize biotinylated proteins (pull down). (**D**) BioID assay of *SPG7*$^{-/-}$ #2 HEK293 transfected with pSPG7-BirA-HA (n = 3 indipendent experiments). WB is revealed by AFG3L2 (positive control), SIRT3, and CS (negative control). (**E**) SIRT3 stability in human control (Ctrl) and *SPG7*_del fibroblasts. Cells were treated with cycloheximide CHX (50 μg/ml) and harvested at indicated time points. Subsequently, immunoblotting against paraplegin, SIRT3 and actin as control was performed. SIRT3 levels were normalized on actin levels and the results are reported in the graph. (n = 3 indipendent experiments; Bayes >3).

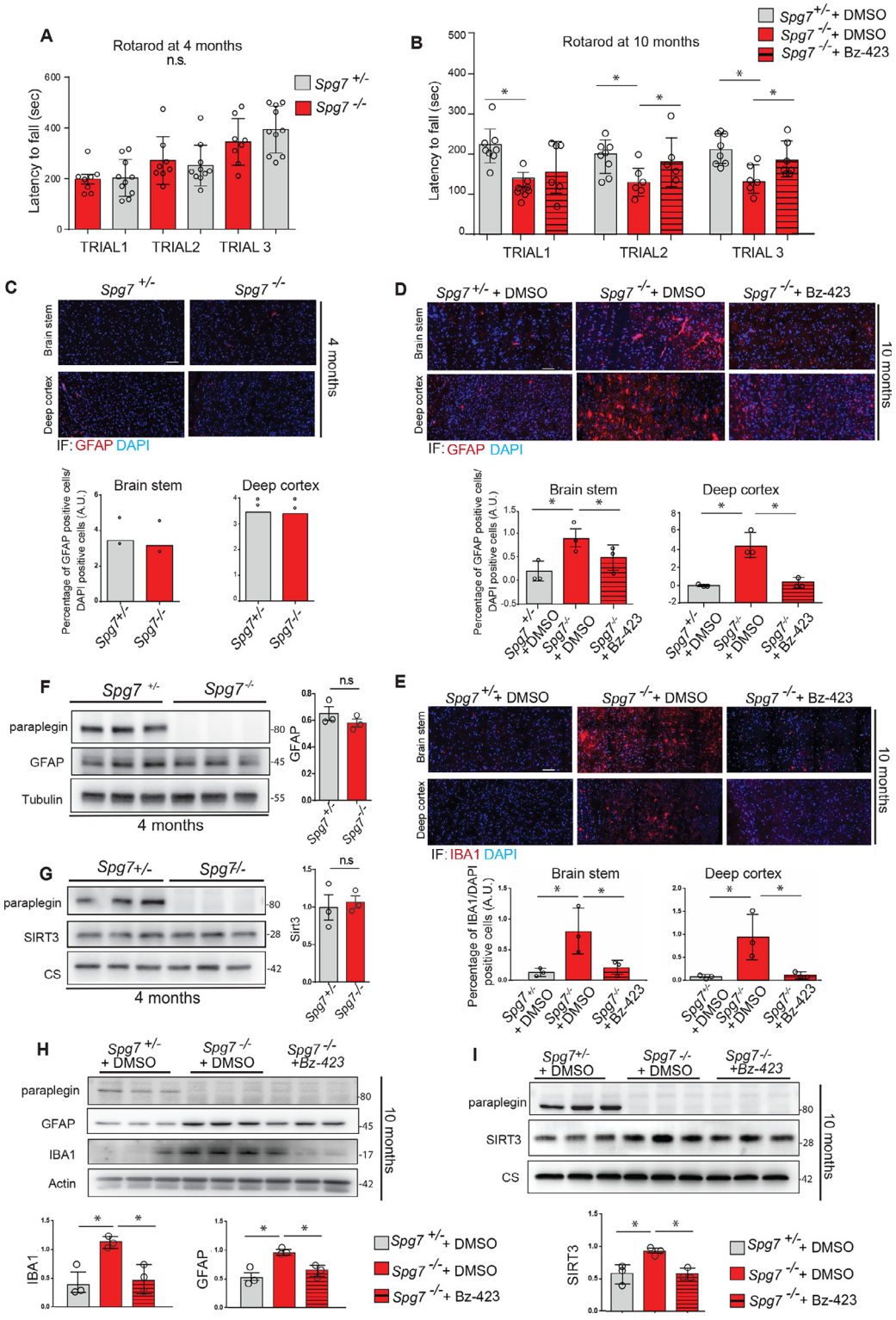

Fig. 7. The SPG7 mouse motor impairment can be normalized by Bz-423 administration.

(**A**) Motor performance of *Spg7*$^{+/-}$ and *Spg7*$^{-/-}$ mice on accelerating rotarod apparatus at 4 months (*Spg7*$^{+/-}$ n = 8 vs *Spg7*$^{-/-}$ n = 10; one-way ANOVA p = n.s) and (**B**) *Spg7*$^{+/-}$, *Spg7*$^{-/-}$ and *Spg7*$^{-/-}$ treated with Bz-423 mice at 10 months of age (*Spg7*$^{+/-}$ n = 8 vs *Spg7*$^{-/-}$ n = 7; *Spg7*$^{-/-}$ plus Bz-423 n = 6; one-way ANOVA $^{*}p<0.05$). (**C**) Epi-fluorescent images (x10) of brain stem and deep cortex slices immunostained with GFAP and DAPI derived from 4-month-old *Spg7*$^{-/-}$ and *Spg7*$^{+/-}$ mice (n = 2/group). (**D**) Same of (**C**) for *Spg7*$^{+/-}$, *Spg7*$^{-/-}$ and *Spg7*$^{-/-}$ treated with Bz-423 mice at 10 months of age (n = 3/group; one-way ANOVA $^{*}p<0.05$). Scale bar, 50 μm. (**E**) Epi-fluorescent images (x10) of brain stem and deep cortex slices immunostained with IBA1 and DAPI derived from 10-month-old *Spg7*$^{-/-}$ and *Spg7*$^{+/-}$ and *Spg7*$^{-/-}$ mice treated with Bz-423 (n = 3/group; one-way ANOVA $^{*}p<0.05$).(**F**) GFAP western blot of mitochondrial lysates isolated from brain of 4 months old *Spg7*$^{+/-}$ and *Spg7*$^{-/-}$ mice (n = 3/group; unpaired Student's t-test). (**G**) SIRT3 western blot of mitochondrial lysates isolated from brain of 4 months old *Spg7*$^{+/-}$ and *Spg7*$^{-/-}$ mice (n = 3/group; unpaired Student's t-test). (**H**) GFAP and IBA1 western blot of mitochondrial lysates isolated from brain of 10 months old *Spg*$^{+/-}$ and *Spg7*$^{-/-}$ mice treated or not with Bz-423 (n = 3/group; one-way ANOVA $^{*}p<0.05$). (**I**) Same of (**G**) for 10 months old *Spg7*$^{+/-}$ and *Spg7*$^{-/-}$ mice treated or not with Bz-423 (n = 3/group; one-way ANOVA $^{*}p<0.05$).

2.31. Study approval and ethics

All studies on animals were conducted in accordance with the institutional guidelines for animal research and approved by the Italian Ministry of Health; Department of Public Health, Animal Health, Nutrition and Food Safety in accordance to the law on animal experimentation (article 7; D.L. 116/92; protocol number: 471/2018-PR; approval date 22/06/2018). Furthermore, all animal treatments were reviewed and approved in advance by the Ethics Committee of TIGEM Institute (Pozzuoli, Italy).

2.32. Role of the funding source

The funding agencies supporting this work did neither participate in the study design, in the collection, analysis and interpretation of data, writing of the manuscript, nor in the final decision to submit the paper.

3. Results

3.1. Increased mitochondrial Ca^{2+}retention capacity and impaired mPTP flickering in SPG7-null cells

We investigate the involvement of paraplegin in mitochondrial Ca^{2+} homeostasis, in human *SPG7* knock-out HEK293 cells (*SPG7*$^{-/-}$ HEK293) (**Figure S1A**) generated by CRISPR/Cas9 genome editing. Calcium retention capacity (CRC) was assayed in WT and *SPG7*$^{-/-}$ cells permeabilized with digitonin and exposed to sequential Ca^{2+} pulses (see Material and Methods). Under this condition, mitochondria take up Ca^{2+} until its concentration in the matrix reaches a critical threshold that induces the opening of the mPTP.

As shown in **Fig. 1A and S1B**, *SPG7*$^{-/-}$ HEK293 required a higher number of Ca^{2+} pulses before developing the sudden increase of extramitochondrial Ca^{2+} concentration that marks the onset of Ca^{2+} release from the mitochondrial matrix, suggesting that the absence of paraplegin increases resistance to mPTP opening. The rise in matrix Ca^{2+} concentration was not significantly different in the two genotypes (**Figure S1C**), suggesting that the decreased Ca^{2+} sensitivity of the mPTP is not due to a higher matrix buffering capacity.

Since mPTP opening is also favored by ROS [52] and since in SPG7 patient cells we reported a defect of respiratory complex I [9], a condition that facilitates increased ROS levels, we tested the CRC in the presence of rotenone, a complex I inhibitor, to blunt the complex I-associated ROS component and inhibits pore opening [53]. Again, the CRC was elevated in *SPG7*$^{-/-}$ HEK293 cells, indicating that in the absence of paraplegin the mPTP is desensitized to Ca^{2+} (**Fig. 1A and S1B**).

These data suggest a dysregulation of the physiologic transient openings of mPTP [54,55] in paraplegin-depleted mitochondria. We tested this hypothesis by labeling mitochondria with both MitoGreen, a specific dye for these organelles, and TMRM, a cationic fluorescent probe, which dynamically accumulates in the mitochondrial matrix in a $\Delta\psi$-dependent manner and has been widely used as indirect indicator of mPTP openings in living cells [56].

In **Fig. 1B**, the mitochondrial network appears yellow at t_0 (overlapping of red and green signals), becomes green at t_1 (loss of TMRM signal caused by the drop in $\Delta\psi$ due to mPTP opening) and then returns yellow when $\Delta\psi$ is restored (t_2 and t_3). To quantify all flickering events per microscope field in a specific time window, we set up an integrated experimental and computational approach for quantitative detection, spatial visualization and frequency analysis of live imaging of mitochondrial flickering as described in Materials and Methods.

By this approach we capture all flickering events that occur in 1 s time interval and visualize them by a 3D surface plot (**Fig. 1C**). To better describe and quantify the fast occurrence of these mPTP opening events, we considered four parameters, i.e. (i) the total amount of exchanged TMRM fluorescence in a single time interval (total TMRM); (ii) the highest peak per field (max TMRM peaks); (iii) the size of the involved mitochondrial area (flickering area/total mito-area); and (iv) the frequency of events (flickering frequency/total mito-area).

The total TMRM exchange was clearly impaired in the SPG7 mutant cells, with lower values and several "zero" scores, which denote the prevalence of mPTP closure in the considered time interval (**Fig. 1D**). Of note, this was not due to difference of membrane potential as shown in patient fibroblasts (**Figure S1D**). Interestingly these data are confirmed in *SPG7*$^{-/-}$ HEK293 and human fibroblasts carrying a large deletion of the *SPG7* gene (*SPG7*_del) [4] (**Figure S1E**) that both displayed a dramatic decrease in all parameters: total TMRM, max peaks, flickering area and frequency (**Fig. 1E, Fig. 1F** and **SVideo1, SVideo2**).

Cyclosporin A (CsA) is an inhibitor of the mPTP, but also inhibits calcineurin [57]. We therefore used its analogue NIM811, which maintains a high affinity for CypD but lacks the inhibitory activity toward calcineurin [41], [58]. When we treated wild type human fibroblasts with NIM811, the flickering activity was abolished, thus confirming that the data obtained by our video analysis can be specifically referred to the activity of mPTP (**Figure S1F**).

Next, we tested the human *SPG7*_del fibroblasts together with four *SPG7* missense mutant cells[59] (**Fig. 1G**), as well as fibroblasts deriving from non-SPG7 forms of HSP, i.e. SPG52 associated to *AP4S1* [60] and SPG31 associated to *REEP1* (F. Santorelli, personal communication) (**Fig. 1H**). We found that significant reduction of mPTP transient opening is present in all *SPG7* mutant cells but not in non-SPG7 HSP cells (**Fig. 1G, 1H and Figure S2A, S2B**), suggesting a pivotal role of paraplegin in the regulation of mPTP opening that is specifically involved in the SPG7 disease mechanism.

3.2. Genetic and pharmacologic rescue of SPG7-dysfunctional mPTP flickering

To test the possible existence of a mechanistic link between SPG7 mPTP flickering defect and the lack of paraplegin activity, we re-expressed paraplegin in *SPG7*_del human fibroblasts. This provided complete rescue of transient mPTP opening to control levels, while expression of a proteolytically inactive form of paraplegin was ineffective (**Fig. 2A and Figure S3A**).

We have shown so far that SPG7$^{-/-}$ cells have a dysfunctional mPTP and inefficient Ca^{2+} homeostasis. Since Ca^{2+} homeostasis by mitochondria is essential in neurons were, at the synapses, Ca^{2+} regulates vesicle recycling and membrane potential maintenance [61], we investigate whether mPTP dysregulation in *Spg7*$^{-/-}$ neurons can be particularly detrimental for synaptic transmission. To assess this, we first excluded differences in membrane potential of cortical neurons (>DIV12) between heterozygous *Spg7*$^{+/-}$ (as control) and *Spg7*$^{-/-}$ mice (**Fig. 2B**).

To test the feasibility of pharmacological correction of the mitochondrial flickering defect, we treated *SPG7*_del cells with Bz-423, a benzodiazepine with known mPTP-sensitizing activity [28]. Remarkably, nanomolar concentration of Bz-423 was sufficient to restore mPTP flickering, thus making this small molecule a good candidate for the development of a therapeutic strategy of SPG7 (**Fig. 2C and Figure S3B**). Strikingly, we found that defective mPTP opening is also a hallmark of *Spg7*$^{-/-}$ cortical neurons (**Fig. 2D**), hence mirroring the behavior observed in SPG7 patient cells, and, more interesting, treatment with Bz-423 was able to rescue the mPTP opening activity in *Spg7*$^{-/-}$ cortical neurons as well (**Fig. 2D** and **Figure S3C**).

3.3. Spg7-null neurons show defective excitatory network activity and synaptic vesicle dynamics

To evaluate the role of paraplegin on the global activity of neuronal networks, we first tested the spontaneous global firing features of primary cultures of cortical neurons from *Spg7*$^{+/-}$ and *Spg7*$^{-/-}$ mice with the multiple electrode array (MEA) approach. Representative raster plots relative to *Spg7*$^{+/-}$ and *Spg7*$^{-/-}$ cultures, in which each timestamp marks an action potential derived from a single electrode, are shown in **Figs. 3A** and **3B**, respectively. Unperturbed neocortex cultures display persistent alternation of silent and active periods [43], which resembles the dynamics of 'up' and 'down' states observed in brain slices [62], as well as *in vivo* [63].

Silent periods are punctuated by network bursts, during which most neurons fire simultaneously. Network bursts are identified as columns in the raster plots of **Fig. 3A** and **3B** and are generally attributed to recurrent excitation [64]. *Spg7*$^{-/-}$ cultures (**Fig. 3B**) presented a decrease of coordinated network activity compared to *Spg7*$^{+/-}$ (**Fig. 3A**), as indicated by the decreased network burst frequency, which is reflected in the observed increase in inter-burst intervals (IBIs**; Figure S4A**). The decrease of coordinated network activity in *Spg7*$^{-/-}$ cultures was accompanied by increased occurrence of unusually prolonged action potential bursts (**Figs. 3B** inset), possibly caused by transient exhaustion of the normal inhibitory feedback on excitatory neurons. The distribution of burst durations is reported in **Figure S4A** (lower panel).

These results show that absence of paraplegin leads to an overall decrease of coordinated network activity, thereby suggesting that alteration of recurrent excitatory connections takes place in *Spg7*$^{-/-}$ networks. Indeed, the lower frequency of *Spg7*$^{-/-}$ network bursts was accompanied by a tendency to develop unusually longer clusters of action potentials.

To better define the underlying synaptic mechanisms, we applied FM dye and patch-clamp methods. Proper dynamics of synaptic vesicles determine effective synaptic transmission. To test whether the altered mPTP flickering caused by paraplegin deficiency influences the exo-endocytic cycle of synaptic vesicles, we exposed *Spg7*$^{+/-}$ and *Spg7*$^{-/-}$ cortical neurons to the styryl FM dye 1−43 during evoked synaptic activity [47,48].

First, we stimulated cultured neurons with high K^+ to promote vesicle exocytosis and subsequent FM1−43 internalization during endocytosis. As shown in **Fig. 3C**, this procedure led to considerably fewer fluorescently labeled vesicles in *Spg7*$^{-/-}$ neurons. This result recalls the data obtained by the MEA test and suggests that *Spg7*$^{-/-}$ neurons display impaired exocytosis, endocytosis, or both. Next, vesicle exocytosis was stimulated and monitored by following the time course of FM1−43 fluorescence decrease. Exocytosis rate was also significantly attenuated in mutant neurons, suggesting a presynaptic imbalance of vesicle dynamics (**Fig. 3D**). Once more, Bz-423 administration to mutant *Spg7*$^{-/-}$ neurons restored the normal vesicle exocytosis (**Fig. 3C and D**), highlighting the functional link between mPTP opening, Ca^{2+} homeostasis and synaptic transmission.

3.4. SPG7-associated pre-synaptic dysfunction is efficiently rescued by Bz-423 administration

The effects of deleting *Spg7* on synaptic function were further investigated by measuring the spontaneous excitatory postsynaptic current (EPSC) amplitude and frequency in primary neocortical cultures from *Spg7*$^{+/-}$ and *Spg7*$^{-/-}$ mice.

Specifically, 78% of *Spg7*$^{-/-}$ neurons show period of EPSC higher frequency that was observed in less than 30% of *Spg7*$^{+/-}$ and *Spg7*$^{-/-}$ neurons pretreated with Bz-423 (**Figure S4B**). Of note, the median EPSC amplitude calculated during the same period was approximately 35% lower in *Spg7*$^{-/-}$ neurons. Once again, Bz-423 rescued the effect of paraplegin loss on the EPSC amplitudes (**Fig. 3E**).

The overall decrease in EPSC amplitude in the *Spg7*$^{-/-}$ genotype is consistent with the results obtained with FM1−43 and could explain the lower frequency of network bursts observed with MEA. These results support a lower steady-state excitatory activity in mutant homozygous cultures caused by a partial exhaustion of synaptic release after bouts of paroxysmal activity, associated with an altered modulation of Ca^{2+}-dependent synaptic vesicle recycling.

To better control the timing of network overstimulation, we applied 100 μM 4-aminopyridine (4-AP) to block voltage-gated K^+ channels. In both *Spg7*$^{+/-}$ and *Spg7*$^{-/-}$ neurons, EPSC amplitudes decreased between the 2nd and the 5th min after 4-AP application, consistent with the synaptic depression usually observed on hyperstimulation [65]. In *Spg7*$^{+/-}$ neurons the average EPSC amplitude decreased from 106 ± 30 pA (2nd min) to 53.7 ± 1.7 pA (5th min), while in *Spg7*$^{-/-}$ neurons it decreased from 81 ± 8.6 pA to 53.3 ± 8.2 pA. However, a different response pattern was observed for EPSC frequency. Representative examples are shown in **Figure S4C** for *Spg7*$^{+/-}$ (top panel) and *Spg7*$^{-/-}$ (bottom panel) neurons. The results of three neuronal cultures obtained from three mice of either genotype are displayed in **Fig. 3F**. Specifically, in *Spg7*$^{+/-}$ neurons, 4-AP brought the average frequency of EPSCs from to 24.1 ± 4.25 Hz (2nd min of application) to 12.5 ± 2.2 Hz (5th min). Conversely, in *Spg7*$^{-/-}$ neurons the EPSC frequency scarcely changed between the 2nd (37.8 ± 6.95 Hz), and the 5th min of 4-AP application (37.1 ± 9 Hz).

We conclude that during synaptic overstimulation the altered functionality of mPTP impairs the compensatory response normally produced by the mitochondrial Ca^{2+} buffering capacity. This is reflected in the inability to control the time course of synaptic release during paroxysmal activation (**Figs. 3F** and **S4C**). This would also explain the general decrease in EPSC amplitudes of *Spg7*$^{-/-}$ neurons. Importantly, these detrimental effects can be significantly ameliorated by Bz-423 administration (**Figs. 3E** and **S4B**).

We next studied the effect of *Spg7* deletion on the spontaneous miniature EPSCs (mEPSCs) revealed by applying TTX to block action potential firing. The aim of these experiments was two-fold: (i) to better assess the pre- and postsynaptic components of the SPG7-dependent synaptic alterations; (ii) to appreciate the synaptic effect of impaired mPTP opening and the consequent reduced mitochondrial buffering capacity in conditions of low spontaneous release, which prevents significant vesicle depletion.

The amplitude and frequency of mEPSCs were measured during 5 min continuous recording, i.e. at the steady state (usually reached within 1−2 min of TTX application). Representative current traces are shown in **Figure S4D** and **S4F**. As expected, TTX administration strongly decreased the EPSC amplitude and frequency in both *Spg7*$^{+/-}$ (**Figure S4E**) and *Spg7*$^{-/-}$ neurons (**Figure S4G**). The average mEPSC amplitude and frequency for each genotype is shown in **Figs. 3G** and **3H**, respectively, together with the results obtained from Bz-423 treated *Spg7*$^{+/-}$ and *Spg7*$^{-/-}$ neurons. While mEPSC amplitudes were similar in the different conditions, the mEPSC frequency was significantly higher in *Spg7*$^{-/-}$ neurons, the effect being reversed by Bz-423 (**Fig. 3G and H**). The higher mEPSC frequency in *Spg7*$^{-/-}$ was also observed in neurons treated with 4-AP, suggesting the that the reduced mitochondrial Ca^{2+} buffering capacity is effective on synaptic release even under partial vesicle depletion (**Fig. 3H**). The indication that Bz-423 restores the defective synaptic transmission provides an internal control by indicating that the difference between genotypes is not caused by major differences in synaptic density, which are very unlikely to be rescued within the fast time frame of the response to Bz-423.

Altogether, these results show that under conditions of low release, as was the case in the presence of TTX, the higher levels of unbuffered presynaptic Ca^{2+} lead to increased vesicle release without alterations of synaptic amplitudes; while during stronger synaptic activation presynaptic mPTP impairment leads to synaptic depression.

3.5. Paraplegin-sirtuin 3 interaction drives cyclophilin D activity and mPTP low conductance opening

We then investigated the molecular mechanism underlying paraplegin-dependent mPTP dysfunction. CypD ablation or inhibition is reported to desensitize mPTP opening [66,67,68]. We hypothesized that CypD levels could be lower in *SPG7* mutant cells, causing in turn the decreased frequency of mPTP opening. Contrary to this prediction, *SPG7*$^{-/-}$ HEK293 and SPG7 patient fibroblasts possess similar amounts of CypD (**Fig. 4A** and **4B**).

However, post-translational modifications play an important role in CypD-mediated regulation of mPTP activity. Indeed, acetylated CypD acts as a positive modulator of mPTP opening, whereas its deacetylated form is associated with decreased probability of mPTP opening [62]· [69]. Accordingly, we tested the relative amount of acetyl-CypD by affinity-purifying lysine-acetylated proteins followed by CypD quantification. The clear-cut result showed that paraplegin-null cells harbor a CypD amount equal to controls, but markedly reduced level of acetyl-CypD, which suggests the occurrence of decreased acetylation or increased deacetylation activity in *SPG7* mutant cells (**Fig. 4C**). Interestingly, the same alteration in CypD acetylation state was also found in mitochondria isolated from the brain of *Spg7*$^{-/-}$ mice at 10 months of age (**Figure S5A**).

Protein acetylation in mitochondria is substantially a spontaneous and non-enzymatic event owing to the high concentration of acetyl-CoA [70]. Thus, the acetylation status is mainly regulated by sirtuin-mediated deacetylation. Sirtuin 3 (SIRT3) localizes to mitochondria and is known to deacetylate a variety of substrates including CypD, thus preventing mPTP opening [71-73]. We found that SIRT3 protein amount is two-fold higher in *SPG7*$^{-/-}$ HEK293 cells (**Fig. 4A**), and that an increased amount of SIRT3 is also found in all *SPG7* patient fibroblasts (**Fig. 4B and 4D**) and in cortical neurons from *Spg7*$^{-/-}$ mice (**Fig. 4E**), but not in fibroblasts from patients affected by non-*SPG7* forms of HSP (**Fig. 4F**).

Interestingly, the re-expression of functional paraplegin in *SPG7*$^{-/-}$ HEK293 cells restores the normal protein amount of SIRT3 (**Fig. 4G**). Conversely, by expressing the protease-inactive form of paraplegin (pSPG7 EQ), SIRT3 level remains unaltered (**Fig. 4G**), indicating that SIRT3 level is regulated by the protease activity of paraplegin.

SIRT3 activation is generally associated with mitochondrial antioxidant defense [72]. We hypothesized that upregulation of SIRT3 antagonizes the ROS challenge caused by paraplegin mutations, at least under conditions not requiring high metabolic expenses. Indeed, lack of paraplegin has no influence on mitochondrial ROS level in basal condition as shown by MitoSOX quantification (**Fig. 5A**), likely as a consequent response to SIRT3 increase, which is functionally linked to SOD2 and catalase hyperactivation [74].

Actually, both SOD2 and catalase proteins were increased, suggesting a cellular response to the SPG7-induced increase of ROS challenge (**Fig. 5B**). Consistent with this observation, *SIRT3* knockdown in *SPG7*$^{-/-}$ HEK293 cells reduced SOD2 and catalase to control level (**Fig. 5C**), indicating that SIRT3 mediates the regulation of these two scavenger enzymes also in our cellular models. Finally, SIRT3, SOD2 and catalase upregulation was prevented by expressing wild-type paraplegin, but not the proteolytically inactive form (**Fig. 5D**), hence demonstrating the need of paraplegin protease activity in order to avoid alerting the SIRT3-supervised ROS scavenging system, which is also controlled at the transcriptional level (**Figure S5B** and **S5C**).

We then tested whether paraplegin interacts with SIRT3 using a proximity-dependent labeling technique [40]· [75]. The fusion protein paraplegin-biotin ligase (pSPG7-BirA-HA) properly localizes to mitochondria (**Fig. 6A**), assembles within the m-AAA complex at the expected molecular weight (**Fig. 6B**) and is able to label a number of proteins (**Fig. 6C**), among which, as expected, AFG3L2 was found (**Fig. 6D**). Remarkably, we identified biotinylated SIRT3 (**Fig. 6D**). Moreover, the analysis of SIRT3 protein stability by the cycloheximide chase assay in control and *SPG7*_del fibroblasts showed that, in the latter, the SIRT3 half-life is prolonged compared to control cells (**Fig. 6E**).

This novel result, together with (i) the increased amount of SIRT3 in paraplegin-null cells, (ii) the normalization of SIRT3 level form in paraplegin-null cells by the expression of paraplegin, but not (iii) of the protease inactive form in paraplegin-null cells, proposes that SIRT3 is a paraplegin substrate that is tightly and dynamically regulated by the protease activity of the *m*-AAA heterocomplex. It should be mentioned that, although we focused on the consequences of SIRT3 upregulation on PTP opening because of its importance in cell death, additional effects are possible that will be interesting to investigate.

3.6. The SPG7 mouse motor impairment can be normalized by Bz-423 administration

The SPG7 mouse model shows a late and slowly progressing motor impairment that parallels the patient disease history [5]. To test whether mPTP impairment has a clinical correlate, we analyzed three groups of mice by testing rotarod motor performance. The first group of four−month-old *Spg7*$^{-/-}$ mice do not show any significant defect compared to control mice (**Fig. 7A**).

The second and third groups are respectively composed of six- and ten-month-old *Spg7*$^{-/-}$ mice, untreated and treated with Bz-423 since the presymptomatic age of four months, together with the relative control groups. As expected, the untreated *Spg7*$^{-/-}$ mice display motor impairment at 6 and 10 months of age, while the performance of Bz-423-treated *Spg7*$^{-/-}$ mice is identical to that of control mice (**Fig. 7B and S6A**).

Furthermore, in 6-month-old mice, EM analysis showed the presence of swollen mitochondria in Spg7$^{-/-}$ spinal cord axons, which were consistently saved by the Bz-423 treatment (**Figure S7**), suggesting that the positive effect of the drug on Spg7$^{-/-}$ motor impairment arises from the normalization of mitochondrial function. Reactive gliosis at symptomatic stage in *Spg7*$^{-/-}$mice, as shown by immunostaining (**Fig. 7C and D and S6B)** and western blot (**Fig. 7F and H and S6C**) of glial acidic fibrillary protein (GFAP) and IBA1 (**Fig. 7E and H**), is quenched by the protective effects of Bz-423 administration. It is worth noting that benzodiazepines can act on TSPO [76]· [77], so producing a beneficial effect on activated microglia; if this effect is synergizing with the documented effect of Bz–423 on mPTP needs further investigation.

Interestingly, while we observed no different amount of brain SIRT3 between *Spg7*$^{+/-}$ and *Spg7*$^{-/-}$ (**Fig. 7G**) mice at four-month of age, but SIRT3 is remarkably increased in the mutant at 6 and 10 months of age. Again, Bz423 treatment can lower *Spg7*$^{-/-}$ SIRT3 level (**Fig. 7I and S6D**), demonstrating *in vivo* that facilitating transient mPTP opening disarms the SIRT3-mediated detrimental effects.

4. Discussion

In this manuscript we have shown that defective paraplegin causes increased amount of SIRT3 in the mitochondrial matrix, resulting in deacetylation of CypD, a key positive regulator of the mPTP. Since deacetylated CypD has a lower affinity for binding to OSCP, the probability of mPTP opening decreases, causing in turn the impairment of Ca^{2+} homeostasis in the nerve terminal and thus impinging upon neurotransmitter release. The mPTP opening defect is rescued by Bz-423, a small molecule mimicking the effect of CypD through binding to the same site on OSCP. This pharmacological bypass prevents the detrimental effects of the lack of paraplegin activity and normalizes the synaptic response *in vitro* and motor deficit *in vivo*. These results also clearly document a physiological role for

mPTP flickering events, and their importance in regulation of Ca^{2+} transients in the nerve terminal.

The involvement of mitochondria in the onset and progression of neurodegenerative diseases is increasingly taking the scene of molecular mechanisms owing to the critical functions performed by the organelle, including ATP synthesis and Ca^{2+} homeostasis, which sustain and safeguard neuronal life [78]. Being a highly compartmentalized organelle, the mitochondrion is endowed with a variety of protein quality control systems in each compartment. In particular, the matrix side of the inner membrane is actively patrolled by *m*-AAA complexes.

In human mitochondria, AFG3L2 and paraplegin can assemble to form the AFG3L2 homopolymeric and the AFG3L2-paraplegin heteropolymeric *m*-AAA complexes. When mutated, these complexes cause two distinct neurodegenerative diseases (SCA28 and SPG7) by targeting specific neuronal populations, i.e. Purkinje cells and upper motoneurons, respectively [4,13,16]. The basis for the neuronal specificity of these diseases may lie in precise differences of substrate and/or function of the two *m*-AAA complexes, although AFG3L2 mutations affect both homo- and hetero-polymeric complexes.

A specific role on the assembly of the mitochondrial Ca2+ uniporter MCU has been assigned to*m*-AAA through the protease control of the regulatory subunit EMRE [79, 80], mainly due to the AFG3L2 subunit.

Here we have shown that the intimate pathogenic mechanism of SPG7, which originates from loss of function of paraplegin, proceeds through activation of SIRT3-mediated defense program and results in decreased physiologic mPTP opening, causing in turn mismanagement of synaptic vesicles and subsequent ineffective post-synaptic stimulation.

A possible association between paraplegin and mPTP opening has been suggested [81 [82]. Subsequent work, however, has demonstrated that m-AAA proteases are essential for the correct assembly of the mitochondrial Ca^{2+} uniporter [79,80 [82], suggesting that the *m*-AAA effect is probably indirect. Furthermore, the mPTP is not affected by genetic manipulation of *SPG7*, ruling out its direct participation in mPTP formation [83].

Our CRC experiment definitely confirms such link by showing that cells lacking paraplegin tolerate larger mitochondrial Ca^{2+} loads before opening of the mPTP. In the past, much emphasis has been placed in defining the conditions and effects of long-lasting opening of mPTP [84], an event associated with release of mitochondrial matrix solutes and of intermembrane proteins including cytochrome *c*, which eventually may result in cell death. A major effort has therefore been devoted to the search of mPTP inhibitors to treat myocardial infarction, ischemia-reperfusion injury, muscular dystrophy, multiple sclerosis/EAE [78]· [85].

However, it has also been proposed that transient openings of mPTP (flickering) have a role in cellular Ca^{2+} homeostasis by providing mitochondria with an effective pathway for fast Ca^{2+} release, a hypothesis that is supported by increasing evidence [32]· [86]· [87]. If this transient opening of mPTP has to be assimilated to mitoflashes, given their common sensitivity to ROS [55]· [88]· [89] remains to be investigated.

Here, we have demonstrated for the first time that impairment of transient pore opening is a causative event in neurodegeneration due to mutations of the *SPG7* gene. Indeed, by evaluating mPTP flickering through the associated changes of mitochondrial TMRM fluorescence with high temporal and spatial resolution, we found that *SPG7* knock-out cells, as well as fibroblasts from patients carrying different paraplegin mutations, display a reduced propensity to mPTP transient opening. This is evident considering both the amount of TMRM molecules exiting the mitochondrion per single pore opening event and the organellar area involved in the single transient. The reduced frequency and size of flickering events in *SPG7* mutants are completely reverted by expression of catalytically active paraplegin.

Non-*SPG7* HSP cells do not show the same significant differences, thus suggesting a specific regulatory role of paraplegin on mPTP. Remarkably, inhibitors of mPTP opening are able to phenocopy SPG7 dysfunction in normal cells, while the mPTP sensitizer Bz-423 [28]· [42] significantly improves the dynamics of mPTP opening in *SPG7*-deficient cells. The availability of the *SPG7* mouse model allowed us to test the occurrence of mPTP and its dynamics also in neuronal cultures, the relevant model to address pathogenic mechanisms of spastic paraplegias. $Spg7^{-/-}$ cortical neurons, similarly to SPG7 patient fibroblasts, showed defective opening of mPTP that was again rescued to normal level by treatment with Bz-423.

Bz-423 was originally identified in the screening of molecules able to selectively kill autoreactive B lymphocytes [90]. Somewhat unexpectedly, the target was identified as the mitochondrial ATP synthase in the unbiased screen of a phage display library [42]. Bz-423 interacts with the OSCP subunit of ATP synthase causing partial inhibition of the enzyme. The interaction results in a conformational change that perturbs the interface between OSCP and the catalytic F_1 sector, disrupting the communication between the latter sector and the peripheral stalk of ATP synthase [91]. Key points for the current discussion are that Bz-423 shares the same binding site on OSCP as the mPTP inducer CypD; and that like CypD it sensitizes the mPTP to Ca^{2+}, thus acting as a pore agonist [28]· [92]. Here we have provided direct evidence that reactivation of mPTP flickering is restored to normal levels by Bz-423 in living cells, hence leaving no doubt that the rescue of neuronal signaling is due to reactivation of the mPTP. This finding demonstrates the crucial role of the physiological mPTP opening for Ca^{2+} homeostasis in neurons.

The high energy-demanding neuronal cells invest most of their energy expenditure for synaptic transmission, in particular at presynaptic terminals, where mitochondria are key players for ensuring an adequate supply of ATP for Ca^{2+} handling and synaptic vesicle dynamics [93]· [94]. Paraplegin loss has an evident effect on the global unperturbed activity of neocortex cultures. $Spg7^{-/-}$ neurons exhibited a marked decrease of network burst frequency together with longer bursts, as seen by MEA experiments, which both suggest a profound rearrangement of network dynamics in the absence of paraplegin.

Synaptic vesicle dynamics clearly shows a consistent decrease of endocytosis and defective exocytosis in $Spg7^{-/-}$ neurons. Impairment of vesicle dynamics is confirmed by the decrease in the amplitude of spontaneous EPSCs, which also explains the reduced frequency of network burst at MEA. Since the synaptic vesicle cycle is tightly controlled by the cytosolic Ca^{2+} concentration, vesicle cycling appears to be highly dependent on mitochondrial function. Indeed, presynaptic mitochondria can rapidly take up Ca^{2+} and thus decrease the probability of synaptic vesicle release, thereby accelerating recovery of neurotransmission after nerve stimulation. We therefore assume that a presynaptic mPTP-associated Ca^{2+} derangement affects vesicle dynamics and limits vesicle release after paroxysmal activity. Once more, Bz-423 pre-treatment of mutant neuronal cultures abolishes the mutant impairment.

Of note, the control spontaneous EPSC frequency halves after overstimulating synaptic activity by 4-AP, while it remains unchanged and higher than control in $Spg7^{-/-}$ cortical neurons. We envisage that, by synaptic overstimulation, the trifling opening propensity of mPTP associated to the defect of paraplegin yields a higher intramitochondrial Ca^{2+} concentration, which eventually limits the capacity of organellar Ca^{2+} buffering and allows locally higher Ca^{2+} concentrations to be reached at the presynaptic terminal, a working hypothesis that is under active investigation.

To better distinguish the pre- and postsynaptic components of the paraplegin-associated defect, we studied mEPSC events under Na^{+} channel inhibition by TTX. The $Spg7^{-/-}$ average mEPSC amplitude is similar to that of the controls, which argues against a major alteration of the postsynaptic response. On the contrary, the higher mEPSC

frequency in *Spg7*$^{-/-}$ cortical neurons suggests again that the disturbed regulation of mPTP causes a higher steady-state free Ca^{2+} level at presynaptic terminal, thus favoring vesicle release. Bz-423, as for several other parameters, restores *Spg7*$^{-/-}$ mEPSC frequency.

Robust and repetitive activation of the *Spg7*$^{-/-}$ presynaptic terminals would generate smaller spontaneous EPSC currents, because of a partial synaptic depression. This interpretation is consistent with the results obtained by pharmacologic inhibition of mitochondrial Ca^{2+} uptake, which accelerates synaptic depression by depleting the pool of available synaptic vesicles [94]· [95]. Our results with FM1-43 suggest that these effects may be accompanied by a decreased efficacy of vesicle recycling.

With the aim of closing the mechanistic gap between paraplegin and mPTP, which is now established as a conformer of ATP synthase [92], we investigated CypD and found a dramatic reduction of its acetylated form, the active species that prompts mPTP opening [71]. In fact, the deacetylase SIRT3 [71]· [72] amount is increased in *SPG7*$^{-/-}$ HEK293 cells, in all *SPG7* patient fibroblasts and in *Spg7*$^{-/-}$ cortical neurons.

We previously reported that SPG7 patient fibroblasts, while behaving normally in control conditions, show an increased susceptibility to oxidative damage when exposed to hydrogen peroxide [9]. Also, we demonstrate here that in basal conditions SPG7 mutant cells display normal level of ROS. Therefore, we suggest that the lack of paraplegin function causes proteostasis stress and decreased complex I activity [9], which generates ROS that are counterbalanced by the general antioxidant program involving rapid SIRT3 activation [72] and then increase of SOD2 and catalase [74]. Indeed, in *SPG7*$^{-/-}$ HEK293 cells both SOD2 and catalase increased, returning to normal levels after inhibition of SIRT3 by siRNA. It is worth noting that expression of paraplegin, but not of its protease inactive form, normalizes SIRT3 expression in SPG7 mutant cells. This suggest that SIRT3 is *bona fide* a substrate of paraplegin, or that the protease activity of paraplegin is essential for regulating SIRT3 level, as supported by the paraplegin-dependent biotinylation of SIRT3 and the increased SIRT3 half-life in the absence of paraplegin.

SIRT3 has other important functional effects in mitochondria and serves as metabolic stress regulator by deacetylating key proteins of the Krebs cycle, of amino acid metabolism and of the electron transfer chain [73]· [96-98]. We propose that loss or mutations of paraplegin cause upregulation of SIRT3, which promptly lowers ROS levels and sustains the metabolic adaptation that follows dysregulation of proteostasis. In SPG7 mutant mitochondria the emergency-driven SIRT3 increase cannot be controlled by paraplegin, and the SIRT3-associated defense program remains “on”.

While the activated antioxidant system is effective in normalizing ROS emergency in SPG7 mutant cells (at least in basal conditions) the high level of SIRT3 activity results in deacetylation of CypD and, finally, in reduced mPTP opening propensity, which translates into the rare occurrence of flickering events. Therefore, we conclude that the lack of regulation of SIRT3 protein by paraplegin in SPG7 cells maintains constitutive high levels of SIRT3 impinging on the mPTP.

The novelty of functionally linking mPTP to SPG7 disease mechanism opens to mPTP modulation as a prospective strategy for SPG7 treatment. The Bz-423 efficacy in annulling the motor impairment of the SPG7 mouse model puts forward that mPTP opening inducers can represent a pharmacological approach to relieve specific mitochondrial conditions. Indeed Bz-423 administration restores the mPTP physiological opening, bypassing the deleterious effect of SIRT3 increase and shows also positive effects on neuroinflammation.

As summarized in the **graphical abstract**, all these results show for the first time that physiological, transient mPTP openings act as important regulators of nerve communication by controlling synaptic vesicle dynamics at the presynaptic terminal through Ca^{2+} management; and that paraplegin mutations have detrimental effects on synaptic transmission through a circuit involving CypD deacetylation. Most importantly, we could reactivate mPTP activity with Bz-423, which was also effective *in vivo* by completely rescuing the SPG7 motor impairment in the animal model. This set of findings thus opens to novel therapeutic avenues to treat SPG7 spastic paraplegia.

Contributors

IS and FM performed *in vivo* and *in vitro* experiments on mPTP activity, molecular analysis and manuscript writing. IS and FM contributed equally.

FGu, SM, and AB, performed and discussed electrophysiology experiments.

LC contributed on CRC setup and general discussion of results.

MCa performed mitochondrial free calcium determination.

GD and AQ analyzed spinal cords of control and *Spg7* mutants by EM.

LP assisted *in vivo* mice testing.

AC and AI performed the statistical analyses.

FS contributed patient cells and general discussion.

FC and FGr, CRC setup, paper discussion and writing.

PB critical strategic discussion and paper writing.

GC supervised experimental phases, paper strategy and writing.

Declaration of Competing Interest

We declare no conflict of interest.

Acknowledgments

We thank Leopoldo Staiano for critical discussion, Maurizio De Fusco for obtaining the *SPG7*$^{-/-}$ HEK293 clones, and Barbara Tumaini for FACS-sorter assistance. This work was supported by, and we are grateful to, Telethon Foundation (TIGEM grant) and Dept. of Defense, US Army (grant W81XWH-18-1-0001), University of Milano-Bicocca (FAR 2018). SM is a recipient of a post-doctoral fellowship awarded by the University of Milano-Bicocca.

Data Sharing Statement

All reagents used in this work are available upon request and a brief statement describing the purpose for their use.

Supplementary materials

Supplementary material associated with this article can be found, in the online version, at doi:10.1016/j.ebiom.2020.103050.

References

[1] Ruano L, Melo C, Silva MC, Coutinho P. The global epidemiology of hereditary ataxia and spastic paraplegia: a systematic review of prevalence studies. Neuroepidemiology 2014;42(3):174–83.
[2] Schule R, Wiethoff S, Martus P, Karle KN, Otto S, Klebe S, et al. Hereditary spastic paraplegia: clinicogenetic lessons from 608 patients. Ann Neurol 2016;79(4):646–58.
[3] Shribman S, Reid E, Crosby AH, Houlden H, Warner TT. Hereditary spastic paraplegia: from diagnosis to emerging therapeutic approaches. Lancet Neurol 2019;18(12):1136–46.
[4] Casari G, De Fusco M, Ciarmatori S, Zeviani M, Mora M, Fernandez P, et al. Spastic paraplegia and OXPHOS impairment caused by mutations in paraplegin, a nuclear-encoded mitochondrial metalloprotease. Cell 1998;93(6):973–83.
[5] Ferreirinha F, Quattrini A, Pirozzi M, Valsecchi V, Dina G, Broccoli V, et al. Axonal degeneration in paraplegin-deficient mice is associated with abnormal mitochondria and impairment of axonal transport. J Clin Invest 2004;113(2):231–42.
[6] Langer T. AAA proteases: cellular machines for degrading membrane proteins. Trends Biochem Sci 2000;25(5):247–51.
[7] Koppen M, Metodiev MD, Casari G, Rugarli EI, Langer T. Variable and tissue-specific subunit composition of mitochondrial m-AAA protease complexes linked to hereditary spastic paraplegia. Mol Cell Biol 2007;27(2):758–67.

[8] Arlt H, Steglich G, Perryman R, Guiard B, Neupert W, Langer T. The formation of respiratory chain complexes in mitochondria is under the proteolytic control of the m-AAA protease. Embo J 1998;17(16):4837–47.
[9] Atorino L, Silvestri L, Koppen M, Cassina L, Ballabio A, Marconi R, et al. Loss of m-AAA protease in mitochondria causes complex I deficiency and increased sensitivity to oxidative stress in hereditary spastic paraplegia. J Cell Biol 2003;163(4):777–87.
[10] Maltecca F, Aghaie A, Schroeder D. The mitochondrial protease AFG3L2 is essential for axonal development. J Neurosci 2008.
[11] Nolden M, Ehses S, Koppen M, Bernacchia A, Rugarli EI, Langer T. The m-AAA protease defective in hereditary spastic paraplegia controls ribosome assembly in mitochondria. Cell 2005;123(2):277–89.
[12] Ehses S, Raschke I, Mancuso G, Bernacchia A, Geimer S, Tondera D, et al. Regulation of OPA1 processing and mitochondrial fusion by m-AAA protease isoenzymes and OMA1. J Cell Biol 2009;187(7):1023–36.
[13] Di Bella D, Lazzaro F, Brusco A, Plumari M, Battaglia G, Pastore A, et al. Mutations in the mitochondrial protease gene AFG3L2 cause dominant hereditary ataxia SCA28. Nat. Genet. 2010;42(4):313–21.
[14] Maltecca F, Magnoni R, Cerri F, Cox G. Haploinsufficiency of AFG3L2, the gene responsible for spinocerebellar ataxia type 28, causes mitochondria-mediated Purkinje cell dark degeneration. J Neurosci 2009.
[15] Maltecca F, De Stefani D, Cassina L, Consolato F, Wasilewski M, Scorrano L, et al. Respiratory dysfunction by AFG3L2 deficiency causes decreased mitochondrial calcium uptake via organellar network fragmentation. Hum Mol Genet 2012;21(17):3858–70.
[16] Maltecca F, Baseggio E, Consolato F, Mazza D, Podini P, Young Jr. SM, et al. Purkinje neuron Ca2+ influx reduction rescues ataxia in SCA28 model. J Clin Invest 2015;125(1):263–74.
[17] Tulli S, Del Bondio A, Baderna V, Mazza D, Codazzi F, Pierson TM, et al. Pathogenic variants in the AFG3L2 proteolytic domain cause SCA28 through haploinsufficiency and proteostatic stress-driven OMA1 activation. J Med Genet 2019.
[18] Pierson TM, Adams D, Bonn F, Martinelli P, Cherukuri PF, Teer JK, et al. Whole-Exome Sequencing Identifies Homozygous AFG3L2 Mutations in a Spastic Ataxia-Neuropathy Syndrome Linked to Mitochondrial m-AAA Proteases. PLoS Genet 2011;7(10):e1002325.
[19] Wedding IM, Koht J, Tran GT, Misceo D, Selmer KK, Holmgren A, et al. Spastic paraplegia type 7 is associated with multiple mitochondrial DNA deletions. PLoS ONE 2014;9(1):e86340.
[20] Pfeffer G, Gorman GS, Griffin H, Kurzawa-Akanbi M, Blakely EL, Wilson I, et al. Mutations in the SPG7 gene cause chronic progressive external ophthalmoplegia through disordered mitochondrial DNA maintenance. Brain 2014;137(Pt 5):1323–36.
[21] Eisner V, Picard M, Hajnoczky G. Mitochondrial dynamics in adaptive and maladaptive cellular stress responses. Nat Cell Biol 2018;20(7):755–65.
[22] DiMauro S, Schon EA. Mitochondrial disorders in the nervous system. Annu Rev Neurosci 2008;31:91–123.
[23] Chen H, Chan DC. Mitochondrial dynamics–fusion, fission, movement, and mitophagy–in neurodegenerative diseases. Hum Mol Genet 2009;18(R2):R169–76.
[24] Gonzalez-Sanchez P, Satrustegui J, Palau F, Del Arco A. Calcium Deregulation and Mitochondrial Bioenergetics in GDAP1-Related CMT Disease. Int J Mol Sci 2019;20(2).
[25] Kang HC, Lee YM, Kim HD. Mitochondrial disease and epilepsy. Brain Dev 2013;35(8):757–61.
[26] Tang J, Oliveros A, Jang MH. Dysfunctional Mitochondrial Bioenergetics and Synaptic Degeneration in Alzheimer Disease. Int Neurourol J 2019;23(Suppl 1):S5–10.
[27] Kramer ML, Schulz-Schaeffer WJ. Presynaptic alpha-synuclein aggregates, not Lewy bodies, cause neurodegeneration in dementia with Lewy bodies. J Neurosci 2007;27(6):1405–10.
[28] Giorgio V, von Stockum S, Antoniel M, Fabbro A, Fogolari F, Forte M, et al. Dimers of mitochondrial ATP synthase form the permeability transition pore. Proc Natl Acad Sci U S A 2013;110(15):5887–92.
[29] Petronilli V, Penzo D, Scorrano L, Bernardi P, Di Lisa F. The mitochondrial permeability transition, release of cytochrome c and cell death. Correlation with the duration of pore openings in situ. J Biol Chem. 2001;276(15):12030–4.
[30] Damiano M, Starkov AA, Petri S, Kipiani K, Kiaei M, Mattiazzi M, et al. Neural mitochondrial Ca2+ capacity impairment precedes the onset of motor symptoms in G93A Cu/Zn-superoxide dismutase mutant mice. J Neurochem 2006;96(5):1349–61.
[31] Elrod JW, Wong R, Mishra S, Vagnozzi RJ, Sakthievel B, Goonasekera SA, et al. Cyclophilin D controls mitochondrial pore-dependent Ca(2+) exchange, metabolic flexibility, and propensity for heart failure in mice. J Clin Invest 2010;120(10):3680–7.
[32] Barsukova AG, Bourdette D, Forte M. Mitochondrial calcium and its regulation in neurodegeneration induced by oxidative stress. Eur J Neurosci 2011;34(3):437–47.
[33] Parone PA, Da Cruz S, Han JS, McAlonis-Downes M, Vetto AP, Lee SK, et al. Enhancing mitochondrial calcium buffering capacity reduces aggregation of misfolded SOD1 and motor neuron cell death without extending survival in mouse models of inherited amyotrophic lateral sclerosis. J Neurosci 2013;33(11):4657–71.
[34] Lu X, Kwong JQ, Molkentin JD, Bers DM. Individual cardiac mitochondria undergo rare transient permeability transition pore openings. Circ Res 2016;118(5):834–41.
[35] Agarwal A, Wu PH, Hughes EG, Fukaya M, Tischfield MA, Langseth AJ, et al. Transient opening of the mitochondrial permeability transition pore induces microdomain calcium transients in astrocyte processes. Neuron 2017;93(3) 587-605 e7.
[36] Bernardi P, Rasola A, Forte M, Lippe G. The mitochondrial permeability transition pore: channel formation by f-atp synthase, integration in signal transduction, and role in pathophysiology. Physiol Rev 2015;95(4):1111–55.
[37] Giorgio V, Burchell V, Schiavone M, Bassot C, Minervini G, Petronilli V, et al. Ca(2+) binding to F-ATP synthase beta subunit triggers the mitochondrial permeability transition. EMBO Rep 2017;18(7):1065–76.
[38] Schneider CA, Rasband WS, Eliceiri KW. NIH Image to ImageJ: 25 years of image analysis. Nat Methods 2012;9(7):671–5.
[39] Lihavainen E, Makela J, Spelbrink JN, Ribeiro AS. Mytoe: automatic analysis of mitochondrial dynamics. Bioinformatics 2012;28(7):1050–1.
[40] Roux KJ, Kim DI, Burke B. BioID: a screen for protein-protein interactions. Curr Protoc Protein Sci 2013;74 Unit 19 23.
[41] Hansson MJ, Mattiasson G, Mansson R, Karlsson J, Keep MF, Waldmeier P, et al. The nonimmunosuppressive cyclosporin analogs NIM811 and UNIL025 display nanomolar potencies on permeability transition in brain-derived mitochondria. J Bioenerg Biomembr 2004;36(4):407–13.
[42] Johnson KM, Chen X, Boitano A, Swenson L, Opipari Jr. AW, Glick GD. Identification and validation of the mitochondrial F1F0-ATPase as the molecular target of the immunomodulatory benzodiazepine Bz-423. Chem Biol 2005;12(4):485–96.
[43] Gullo F, Mazzetti S, Maffezzoli A, Dossi E, Lecchi M, Amadeo A, et al. Orchestration of "presto" and "largo" synchrony in up-down activity of cortical networks. Front Neural Circuits 2010;4:11.
[44] Wagenaar DA, Pine J, Potter SM. Searching for plasticity in dissociated cortical cultures on multi-electrode arrays. J Negat Results Biomed 2006;5:16.
[45] Becchetti A, Gullo F, Bruno G, Dossi E, Lecchi M, Wanke E. Exact distinction of excitatory and inhibitory neurons in neural networks: a study with GFP-GAD67 neurons optically and electrophysiologically recognized on multielectrode arrays. Front Neural Circuits 2012;6:63.
[46] Gullo F, Maffezzoli A, Dossi E, Lecchi M, Wanke E. Classifying heterogeneity of spontaneous up-states: a method for revealing variations in firing probability, engaged neurons and Fano factor. J Neurosci Methods 2012;203(2):407–17.
[47] Gaffield MA, Betz WJ. Imaging synaptic vesicle exocytosis and endocytosis with FM dyes. Nat Protoc 2006;1(6):2916–21.
[48] Lazarenko RM, DelBove CE, Zhang Q. Fluorescent measurement of synaptic activity using FM dyes in dissociated hippocampal cultured neurons. Bio Protoc 2018;8(2).
[49] Aracri P, Meneghini S, Coatti A, Amadeo A, Becchetti A. alpha4beta2(*) nicotinic receptors stimulate GABA release onto fast-spiking cells in layer V of mouse prefrontal (Fr2) cortex. Neuroscience 2017;340:48–61.
[50] Richner M, Jager SB, Siupka P, Vaegter CB. Hydraulic extrusion of the spinal cord and isolation of dorsal root ganglia in rodents. J Vis Exp 2017(119).
[51] Kalaitzis AA, Lawrence ND. A simple approach to ranking differentially expressed gene expression time courses through Gaussian process regression. BMC Bioinformatics 2011;12:180.
[52] Di Lisa F, Bernardi P. Mitochondrial function and myocardial aging. A critical analysis of the role of permeability transition. Cardiovasc Res. 2005;66(2):222–32.
[53] Li B, Chauvin C, De Paulis D, De Oliveira F, Gharib A, Vial G, et al. Inhibition of complex I regulates the mitochondrial permeability transition through a phosphate-sensitive inhibitory site masked by cyclophilin D. Biochim Biophys Acta 2012;1817(9):1628–34.
[54] De Giorgi F, Lartigue L, Ichas F. Electrical coupling and plasticity of the mitochondrial network. Cell Calcium 2000;28(5–6):365–70.
[55] Wang W, Fang H, Groom L, Cheng A, Zhang W, Liu J, et al. Superoxide flashes in single mitochondria. Cell 2008;134(2):279–90.
[56] Blanchet L, Grefte S, Smeitink JA, Willems PH, Koopman WJ. Photo-induction and automated quantification of reversible mitochondrial permeability transition pore opening in primary mouse myotubes. PLoS ONE 2014;9(11):e114090.
[57] Cereghetti GM, Stangherlin A, Martins de Brito O, Chang CR, Blackstone C, Bernardi P, et al. Dephosphorylation by calcineurin regulates translocation of Drp1 to mitochondria. Proc Natl Acad Sci U S A 2008;105(41):15803–8.
[58] Zulian A, Rizzo E, Schiavone M, Palma E, Tagliavini F, Blaauw B, et al. NIM811, a cyclophilin inhibitor without immunosuppressive activity, is beneficial in collagen VI congenital muscular dystrophy models. Hum Mol Genet 2014;23(20):5353–63.
[59] Mancini C, Giorgio E, Rubegni A, Pradotto L, Bagnoli S, Rubino E, et al. Prevalence and phenotype of the c.1529C>T SPG7 variant in adult-onset cerebellar ataxia in Italy. Eur J Neurol 2019;26(1):80–6.
[60] Tessa A, Battini R, Rubegni A, Storti E, Marini C, Galatolo D, et al. Identification of mutations in AP4S1/SPG52 through next generation sequencing in three families. Eur J Neurol 2016;23(10):1580–7.
[61] Mnatsakanyan N, Beutner G, Porter GA, Alavian KN, Jonas EA. Physiological roles of the mitochondrial permeability transition pore. J Bioenerg Biomembr 2017;49(1):13–25.
[62] Lee CF, Chavez JD, Garcia-Menendez L, Choi Y, Roe ND, Chiao YA, et al. Normalization of NAD+ redox balance as a therapy for heart failure. Circulation 2016;134(12):883–94.
[63] Luczak A, Bartho P, Marguet SL, Buzsaki G, Harris KD. Sequential structure of neocortical spontaneous activity in vivo. Proc Natl Acad Sci U S A 2007;104(1):347–52.
[64] Mann EO, Kohl MM, Paulsen O. Distinct roles of GABA(A) and GABA(B) receptors in balancing and terminating persistent cortical activity. J Neurosci 2009;29(23):7513–8.
[65] Zucker RS, Regehr WG. Short-term synaptic plasticity. Annu Rev Physiol 2002;64:355–405.

[66] Nakagawa T, Shimizu S, Watanabe T, Yamaguchi O, Otsu K, Yamagata H, et al. Cyclophilin D-dependent mitochondrial permeability transition regulates some necrotic but not apoptotic cell death. Nature 2005;434(7033):652–8.
[67] Basso E, Fante L, Fowlkes J, Petronilli V, Forte MA, Bernardi P. Properties of the permeability transition pore in mitochondria devoid of Cyclophilin D. J Biol Chem 2005;280(19):18558–61.
[68] Baines CP, Kaiser RA, Purcell NH, Blair NS, Osinska H, Hambleton MA, et al. Loss of cyclophilin D reveals a critical role for mitochondrial permeability transition in cell death. Nature 2005;434(7033):658–62.
[69] Karamanlidis G, Lee CF, Garcia-Menendez L, Kolwicz Jr. SC, Suthammarak W, Gong G, et al. Mitochondrial complex I deficiency increases protein acetylation and accelerates heart failure. Cell Metab 2013;18(2):239–50.
[70] Baeza J, Smallegan MJ, Denu JM. Site-specific reactivity of nonenzymatic lysine acetylation. ACS Chem Biol 2015;10(1):122–8.
[71] Hafner AV, Dai J, Gomes AP, Xiao CY, Palmeira CM, Rosenzweig A, et al. Regulation of the mPTP by SIRT3-mediated deacetylation of CypD at lysine 166 suppresses age-related cardiac hypertrophy. Aging (Albany NY) 2010;2(12):914–23.
[72] Cheng A, Yang Y, Zhou Y, Maharana C, Lu D, Peng W, et al. Mitochondrial SIRT3 mediates adaptive responses of neurons to exercise and metabolic and excitatory challenges. Cell Metab 2016;23(1):128–42.
[73] Yang W, Nagasawa K, Munch C, Xu Y, Satterstrom K, Jeong S, et al. Mitochondrial sirtuin network reveals dynamic SIRT3-dependent deacetylation in response to membrane depolarization. Cell 2016;167(4):985–1000 e21.
[74] Sundaresan NR, Gupta M, Kim G, Rajamohan SB, Isbatan A, Gupta MP. Sirt3 blocks the cardiac hypertrophic response by augmenting Foxo3a-dependent antioxidant defense mechanisms in mice. J Clin Invest 2009;119(9):2758–71.
[75] Li P, Li J, Wang L, Di LJ. Proximity labeling of interacting proteins: application of BioID as a discovery tool. Proteomics 2017;17(20).
[76] Sileikyte J, Blachly-Dyson E, Sewell R, Carpi A, Menabo R, Di Lisa F, et al. Regulation of the mitochondrial permeability transition pore by the outer membrane does not involve the peripheral benzodiazepine receptor (Translocator Protein of 18kDa (TSPO)). J Biol Chem 2014;289(20):13769–81.
[77] Bader S, Wolf L, Milenkovic VM, Gruber M, Nothdurfter C, Rupprecht R, et al. Differential effects of TSPO ligands on mitochondrial function in mouse microglia cells. Psychoneuroendocrinology 2019;106:65–76.
[78] Devine MJ, Kittler JT. Mitochondria at the neuronal presynapse in health and disease. Nat Rev Neurosci 2018;19(2):63–80.
[79] Konig T, Troder SE, Bakka K, Korwitz A, Richter-Dennerlein R, Lampe PA, et al. The m-AAA protease associated with neurodegeneration limits MCU activity in mitochondria. Mol Cell 2016;64(1):148–62.
[80] Tsai CW, Wu Y, Pao PC, Phillips CB, Williams C, Miller C, et al. Proteolytic control of the mitochondrial calcium uniporter complex. Proc Natl Acad Sci U S A 2017;114(17):4388–93.
[81] Shanmughapriya S, Rajan S, Hoffman NE, Higgins AM, Tomar D, Nemani N, et al. SPG7 is an essential and conserved component of the mitochondrial permeability transition pore. Mol Cell 2015;60(1):47–62.
[82] Hurst S, Baggett A, Csordas G, Sheu SS. SPG7 targets the m-AAA protease complex to process MCU for uniporter assembly, Ca(2+)influx, and regulation of mPTP opening. J Biol Chem 2019.
[83] Klutho PJ, Dashek RJ, Song L, Baines CP. Genetic manipulation of SPG7 or NipSnap2 does not affect mitochondrial permeability transition. Cell Death Discov 2020;6:5.
[84] Giorgio V, Guo L, Bassot C, Petronilli V, Bernardi P. Calcium and regulation of the mitochondrial permeability transition. Cell Calcium 2018;70:56–63.
[85] Sileikyte J, Forte M. Shutting down the pore: the search for small molecule inhibitors of the mitochondrial permeability transition. Biochim Biophys Acta 2016;1857(8):1197–202.
[86] Bernardi P, Petronilli V. The permeability transition pore as a mitochondrial calcium release channel: a critical appraisal. J-Bioenerg-Biomembr 1996;28(2):131–8.
[87] Ichas F, Mazat JP. From calcium signaling to cell death: two conformations for the mitochondrial permeability transition pore. Switching from low- to high-conductance state. Biochim Biophys Acta. 1998;1366(1–2):33–50.
[88] Ying Z, Chen K, Zheng L, Wu Y, Li L, Wang R, et al. Transient activation of mitoflashes modulates nanog at the early phase of somatic cell reprogramming. Cell Metab 2016;23(1):220–6.
[89] Fu ZX, Tan X, Fang H, Lau PM, Wang X, Cheng H, et al. Dendritic mitoflash as a putative signal for stabilizing long-term synaptic plasticity. Nat Commun 2017;8(1):31.
[90] Blatt NB, Bednarski JJ, Warner RE, Leonetti F, Johnson KM, Boitano A, et al. Benzodiazepine-induced superoxide signals B cell apoptosis: mechanistic insight and potential therapeutic utility. J Clin Invest 2002;110(8):1123–32.
[91] Stelzer AC, Frazee RW, Van Huis C, Cleary J, Opipari Jr. AW, Glick GD, et al. NMR studies of an immunomodulatory benzodiazepine binding to its molecular target on the mitochondrial F(1)F(0)-ATPase. Biopolymers 2010;93(1):85–92.
[92] Urbani A, Giorgio V, Carrer A, Franchin C, Arrigoni G, Jiko C, et al. Purified F-ATP synthase forms a Ca(2+)-dependent high-conductance channel matching the mitochondrial permeability transition pore. Nat Commun 2019;10(1):4341.
[93] Harris JJ, Jolivet R, Attwell D. Synaptic energy use and supply. Neuron 2012;75(5):762–77.
[94] David G, Barrett EF. Mitochondrial Ca2+ uptake prevents desynchronization of quantal release and minimizes depletion during repetitive stimulation of mouse motor nerve terminals. J Physiol 2003;548(Pt 2):425–38.
[95] Billups B, Forsythe ID. Presynaptic mitochondrial calcium sequestration influences transmission at mammalian central synapses. J Neurosci 2002;22(14):5840–7.
[96] Hirschey MD, Shimazu T, Jing E, Grueter CA, Collins AM, Aouizerat B, et al. SIRT3 deficiency and mitochondrial protein hyperacetylation accelerate the development of the metabolic syndrome. Mol Cell 2011;44(2):177–90.
[97] Ahn BH, Kim HS, Song S, Lee IH, Liu J, Vassilopoulos A, et al. A role for the mitochondrial deacetylase Sirt3 in regulating energy homeostasis. Proc Natl Acad Sci U S A 2008;105(38):14447–52.
[98] Schwer B, Bunkenborg J, Verdin RO, Andersen JS, Verdin E. Reversible lysine acetylation controls the activity of the mitochondrial enzyme acetyl-CoA synthetase 2. Proc Natl Acad Sci U S A 2006;103(27):10224–9.